

Physics-inspired Equivariant Descriptors of Non-bonded Interactions

Kevin K. Huguenin-Dumittan,^{1,*} Philip Loche,^{1,*} Ni Haoran,¹ and Michele Ceriotti^{1,†}

¹*Laboratory of Computational Science and Modeling, IMX,
École Polytechnique Fédérale de Lausanne, 1015 Lausanne, Switzerland*

One essential ingredient in many machine learning (ML) based methods for atomistic modeling of materials and molecules is the use of locality. While allowing better system-size scaling, this systematically neglects long-range (LR) effects, such as electrostatics or dispersion interaction. We present an extension of the long distance equivariant (LODE) framework that can handle diverse LR interactions in a consistent way, and seamlessly integrates with preexisting methods by building new sets of atom centered features. We provide a direct physical interpretation of these using the multipole expansion, which allows for simpler and more efficient implementations. The framework is applied to simple toy systems as proof of concept, and a heterogeneous set of molecular dimers to push the method to its limits. By generalizing LODE to arbitrary asymptotic behaviors, we provide a coherent approach to treat arbitrary two- and many-body non-bonded interactions in the data-driven modeling of matter.

Modeling approaches based on machine learning (ML) have become ubiquitous in the field of atomistic simulations, bridging the gap between techniques purely based on classical mechanics and empirical forcefields, which are fast but less accurate, and quantum mechanical approaches providing greater accuracy at a larger cost [1–4]. Since the introduction of early ML models to predict the energy of extended atomic structures [1, 2] and molecules[5], the field has rapidly expanded in many directions, improving the accuracy of predictions, and extending the diversity of target properties beyond energies and forces, including vectorial and tensorial properties [6–8], electron densities [9–12], single-particle electronic Hamiltonians [13, 14] and many-particles wavefunctions[15, 16]. A key ingredient in most successful approaches has been the use of locality, often justified in terms of the “nearsightedness” of electronic structure [17, 18]. Local models truncate atomic interactions up to a cutoff radius, which allows the development of fast algorithms scaling linearly with the number of particles.

Introducing a cutoff, however, neglects important contributions from all sorts of long-range (LR) interactions. The most prominent LR effects are the $1/r$ Coulomb potential between electrical charges as well as the $1/r^6$ dispersion interactions between induced dipoles [19]. Many other asymptotic decays exist, e.g. charge-dipole and hydrogen bonding ($1/r^2$), permanent dipole-dipole ($1/r^3$), and charge-non-polar ($1/r^4$)[20] interactions. On a coarser-grained scale, the effective potential in dense polymer solutions, between particles and surfaces, or membranes in biological systems involves different combinations of exponents [21, 22].

At the simplest level, neglecting LR effects sets a lower bound to the possible prediction error. In some cases, LR interactions determine qualitatively different behavior in materials [23]. In order to address these issues in

machine learning models, several approaches have been proposed. If the goal is to predict the energy and the forces of an atomic structure, the simplest strategy is to add an explicitly-fitted $1/r^p$ potential baseline. This idea was already applied to one of the earliest ML potentials [2], and can easily be combined with any ML scheme [24–26]. Such a simple approach, in which each chemical species is assigned a fixed point charge, has clear limitations, and more sophisticated techniques have been proposed. One direction is to explicitly include the Wannier centers associated with the valence electrons into the ML framework [27, 28]. Given that the center of charge of the electrons can be different from the positions of the nuclei, these models can describe both ionic charge and local polarization. In order to describe global charge transfer, without violating charge-neutrality constraints, several methods have been proposed that employ a global charge equilibration scheme, predicting electronegativities rather than the charges [29–31], and more generally self-consistent treatment of electrostatics[32]. While the Coulomb potential has been at the center of these developments, some of these methods have also been extended to other interactions, including dispersion [25] and more general potentials [33], often using a rather explicit physics-based functional form. There is, however, a lack of a unifying framework that treats various types of LR interactions consistently. One promising approach to fill in this gap is the Long-Distance Equivariant (LODE) framework[34, 35], that encodes LR structural data in a form that mimics the asymptotic behavior of electrostatic interactions. Thus, even if LODE features are “physics-inspired” – and can be related to explicit physical interactions when used in a linear model – they retain the full flexibility of general ML schemes.

Here, we generalize LODE features to mimic the asymptotic behavior of any potential with an inverse power law form beyond Coulomb interactions, and provide an efficient implementation that also includes gradients of the descriptors with respect to atomic positions, that are needed to compute forces. We provide a detailed mathematical analysis that allows an exact physical in-

* Contributed equally to this work

† michele.ceriotti@epfl.ch

terpretation of the resulting LODE coefficients, and explain how the framework can also describe many-body effects beyond pair potentials. We finally investigate the subtle balance between physical interpretability and generality of the ML model using two families of datasets: simple toy systems and a diverse collection of molecular dimers.

We first provide a concise summary on the construction of the LODE descriptors as is discussed in Refs. 36 and 37, and illustrated in Figure 1. A self-contained and more detailed discussion can be found in section S2 in the Supporting Information. The position of the atoms in a structure is encoded in a permutation-invariant way by defining a smooth atom density $\rho(\mathbf{r})$ – the same that is used to define local atom-density descriptors including the popular smooth overlap of atomic positions (SOAP) descriptor (Figure 1a). The Coulomb potential $V(\mathbf{r})$ generated by this density (Figure 1b) can then be computed efficiently (e.g. with an Ewald summation in reciprocal space[38]). The atom centered features for an atom i are then generated by first shifting the coordinate system to its position \mathbf{r}_i , leading to the atom-centered potential $V_i(\mathbf{r}) = V(\mathbf{r}_i + \mathbf{r})$. This potential, evaluated up to some cutoff radius r_{cut} , is then projected onto a set of basis functions consisting of (real) spherical harmonics Y_l^m specified by the angular indices $l = 0, 1, \dots, l_{\text{max}}$ and $|m| \leq l$, as well as radial basis functions $R_{nl}(r)$ for $n = 0, 1, \dots, n_{\text{max}} - 1$ via the integral

$$V_{i,nlm} = \int_0^{r_{\text{cut}}} d^3\mathbf{r} R_{nl}(r) Y_l^m(\hat{\mathbf{r}}) V_i(\mathbf{r}), \quad (1)$$

where \mathbf{r} corresponds to the displacement from atom i . Due to the slow decay of the $1/r$ potential, these LODE coefficients contain information on the position of far-away atoms, despite using an environment cutoff for the integration. In fact, similarly to a Fourier expansion, knowing all coefficients in the limit as $n_{\text{max}}, l_{\text{max}} \rightarrow \infty$ would allow one to recover the original function V_i , meaning that the LODE coefficients also play a role of fitting coefficients as shown in Figure 1c. They have the same mathematical properties as those used to discretize the local density ρ , and can be used in a similar way, combining them in a symmetry-adapted fashion to obtain invariant features analogous to the SOAP [2, 3] descriptor and its higher-order invariant and equivariant extensions [4, 7, 14, 39, 40]. In particular, it was shown that a combination of local density coefficients and Coulomb-field LODE leads to “multi-scale” features, that, when used in linear models, can be interpreted in relation to the multipole expansion of the electrostatic potential [35].

As a first key result in this work, for which we provide a detailed derivation in sections S1 and S2 in the Supporting Information, we present an exact physical interpretation of the LODE coefficients $V_{i,nlm}$. For a fixed center atom i , the potential $V_i^>(\mathbf{r})$ around atom i generated by the charge density *outside* the cutoff region can

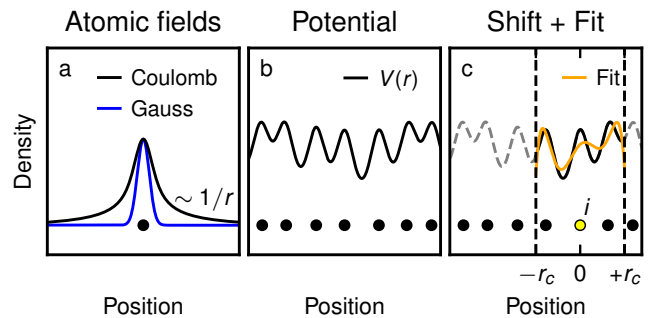


Figure 1. Construction of the LODE features. (a) shows a Gaussian density and the Coulomb potential generated by it, which is a smeared out version of the bare $1/r$ Coulomb potential. The key for the LODE construction is the significantly slower decay of the smeared Coulomb potential. (b) shows the potential field $V(r)$ obtained as the superposition of the smeared Coulomb potential on all atoms (black circles). In panel (c), V_i is defined as the restriction of V to a local environment around the position of atom i (yellow circle), where the coordinate system has also been shifted. V_i is then discretized using atom-centered basis functions. The resulting coefficients, obtained from Equation 1, are the LODE features.

be shown to be of the form

$$V_i^>(\mathbf{r}) = \sum_{lm} M_{i,lm}^> r^l Y_l^m(\hat{\mathbf{r}}), \quad (2)$$

where the coefficients $M_{i,lm}^>$ are called (exterior) multipole moments and completely characterize the potential generated by the exterior atoms as discussed in more detail in section S1 of the Supporting Information. The main result here is that with an appropriate choice of radial basis, the LODE coefficients are precisely *equal* to the multipole moments, $V_{i,nlm} = M_{i,lm}^>$, and in particular contain the full information on the exterior atoms for what concerns electrostatic properties. Furthermore, our derivation shows that one does not need a large number n_{max} of basis functions, since Equation 2 does not depend on an index n . By choosing $R_{0l}(r) = r^l$, a single monomial basis function per angular momentum channel l is sufficient to capture the electrostatic contributions from far-field atoms. This translates in computational savings by a factor of n_{max} , which varies between 4 and 12 in typical applications. We will call this the monomial or optimized basis, since this is the most compressed form in which we can store the exterior information.

A potential risk in previous LODE implementations [34, 35], that are fine-tuned to capture electrostatic behavior, is that they will be less flexible in describing other long-range interactions. To address this issue, we generalize the LODE construction to arbitrary $1/r^p$ interactions, leading to a p -dependent family of potentials $V^{(p)}$. While conceptually straightforward, this change does come with several subtleties. First, a key ingredient to obtain well defined coefficients in the Coulombic

case was the use of Gaussian charge densities rather than point charges to remove the singularity of $1/r$ at the origin. For $p \geq 3$, the divergence as $r \rightarrow 0$ becomes so strong that even using a Gaussian smearing, the resulting potential is still singular. Thus, a family of effective potentials parametrized by p and having the correct $1/r^p$ behavior for large distances is used instead of the bare form [38, 41, 42]. The second difference is that the multipole expansion for a $1/r^p$ potential with $p \neq 1$ contains several terms that do not appear in the Coulombic case. Despite these additional complications, all results can still be translated to the general case with suitable modifications. Both of these subtleties are discussed in section S3 in the Supporting Information. While these results apply to interactions that can be treated as pair potentials, the LODE framework can also describe a wide range of LR many-body interactions beyond pair potentials by combining multiple LODE coefficients to generate higher order invariants. This approach, which we discuss in more detail in section S4, leads to the LR analogue of systematic body-order expansions used in methods based on atom-centered density correlations [39], including ACE [40] or NICE [43].

To assess the capabilities of the general LODE framework, we begin with a demonstrative example, using a modified version of the toy dataset originally presented in Ref. 35. It consists of 2000 structures, each obtained by distributing at random 64 particles inside cubic cells of varying size, such that no particles are closer than 2.5 Å. For the same particle positions we consider two different potentials: in one case, similar to Ref. 35, we treat the structures as an overall neutral cloud of ± 1 charges. In the second test, all atoms are equal, and interact via an attractive $1/r^6$ dispersion interaction. Periodic boundary conditions are used in both cases.

The energies of these systems are learned using linear models built either on short-range (SR) or LODE descriptors with $p = 1$ and $p = 6$. The latter are computed with a method similar to Ewald summation using a reciprocal space sum, matching the periodicity of the target system. For the LODE descriptors, we only take the coefficients for which $l = m = 0$, and compare two choices of radial basis functions R_{nl} . As a baseline, we use the Gaussian-type orbital (GTO) basis functions used in Ref. 35 as well as for various SR models including this test, with $n_{\max} = 8$ radial basis functions. This is compared with the optimal radial basis that uses a single basis function. In fact, for $l = m = 0$, both the spherical harmonic $Y_0^0 = 1/\sqrt{4\pi}$ and $R_{0l} = r^l = 1$ are just constant functions. Thus, it can be seen from Equation 1 that the coefficient $V_{i,000}$ that enters the model is, up to a global factor, the average within the cutoff sphere of the potential generated by the atom density. For sufficiently small cutoff radii, we therefore simply recover the potential at the position of atom i . Model details and parameters can be found in section S5 of the Supporting Information.

The results in Figure 2 show the percentage root mean

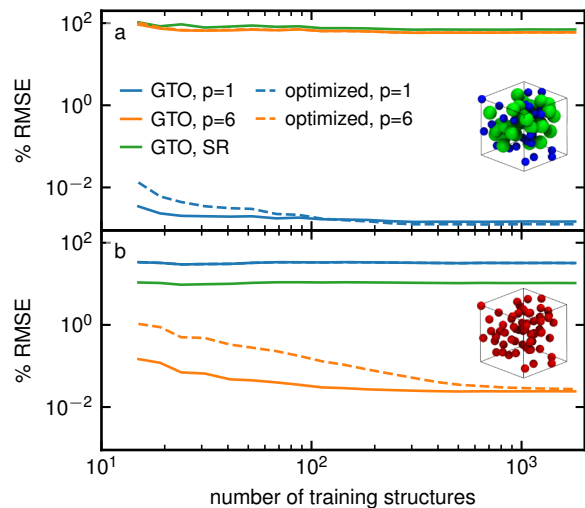


Figure 2. Learning curves showing the validation %RMSE against the number of training structures. In (a), half of the particles each have a charge of ± 1 , while in (b), all particles are neutral and interact solely via an attractive dispersion interaction. Solid lines show models using the GTO basis with $n_{\max} = 8$ coefficients, whereas dashed lines use the optimized basis with a single coefficient. To convert back to absolute errors, the standard deviations in the energies are $\sigma = 1.15$ eV/atom and $\sigma = 0.14$ eV/atom, respectively.

squared error (%RMSE), defined as the absolute RMSE divided by the standard deviation σ of the energy in the training set, against the number of training set structures. We observe that the SR descriptors, even when using a large 9 Å cutoff, are unable to learn electrostatic or dispersion interactions, leading to rapidly-saturating learning curves. On the other hand, the results show clearly how using a generalized LODE descriptor adapted to the asymptotic decay of the LR potential allows to learn the target potential with very high accuracy, and very few training structures. By using the optimized radial basis, a single LODE coefficient can reach the same accuracy of a model using an expansion on $n_{\max} = 8$ GTO basis functions.

In light of the analytical results discussed above, these observations are unsurprising. In fact, it is more insightful to comment on the residual errors. First, it is clear that the choice of a physically constrained model affects its applicability to other types of interactions. The performance of a $V^{(1)}$ linear model for a $1/r^6$ potential, or those of a $V^{(6)}$ for $1/r$ are comparable or worse to those of a SR model. Second, interactions-adapted models achieve high accuracy, but there is a residual error, which is due to the finite Gaussian smearing of the atoms and convergence of the reciprocal space sum in the implementation. While Ewald-based methods in classical molecular dynamics, including PME [44], SPME [45] and P3M [46] correct for the smearing by using a compensating SR part [47], the LODE descriptor itself does not

contain such corrections. This would not be an issue in practice, however, since one typically combines LODE together with SR representations for more complex systems. The slightly slower convergence of the optimized radial basis can also be explained by the finite Gaussian smearing, and the cutoff radius for the integration in Equation (1), leading to discrepancies between the true potential and the LODE coefficients that can be compensated with a sufficient amount of data and/or fitting coefficients.

From this first example, we conclude that a single $l = 0$ component of the extended LODE framework (1) is sufficiently expressive to learn a LR potential with matching exponent with high accuracy and (2) has an increased efficiency due to a better choice of radial basis. Beyond such pair or two-body potentials, we also show in section S4 how higher order invariants built from the LODE coefficients can be used to learn three-body dispersion, supporting the more general result that the framework is also capable of treating many-body LR effects. Armed with descriptors that have a rigorous physical interpretation, but can be easily combined with arbitrary ML frameworks, we can now explore the interplay between descriptors, model architecture, and type of LR interactions using a more challenging dataset, with target properties obtained from actual quantum mechanical methods.

To cover a wide range of interactions between sufficiently simple but relevant molecules, we base our tests, on the BioFragment Database (BFDdb) [35, 48], that contains 2291 pairs created from 22 relaxed organic molecules. For each configuration, we evaluate energies and forces along binding curves built starting from the configuration included in the BFDdb with initial separation r_0 , and increasing the separation along the line connecting the centers of mass (COM) of the two molecules, up to $r = 15 \text{ \AA}$ between the COMs. We note that (1) we use the HSE06 hybrid functional [49] with a high fraction of exact exchange, to reduce the DFT localization error and ensure that charged dimers dissociate without spurious fractional charges, (2) we include a non-local many-body dispersion correction[50] and (3) we use a supercell approach, so that binding energies also contain interactions between periodic replicas, consistent with the reciprocal-space calculation of LODE descriptors. Full details for the dataset construction and the models are provided in section S6 of the Supporting Information.

The BFDdb contains charged molecules, polar molecules with an effectively constant dipole moment, and apolar molecules without any permanent charge or dipole moment. The combination of these three molecular categories results in six dimer classes with different ideal power-law decay constants of their interactions [21]: charge-charge (CC) with $p_{CC} = 1$, charge-polar (CP) with $p_{CP} = 2$, polar-polar (PP) with $p_{PP} = 3$, charge-apolar (CA) with $p_{CA} = 4$, polar-apolar (PA) with $p_{PA} = 5$, and finally apolar-apolar (AA) with an ideal interaction decay of $p_{AA} = 6$. We show an example

snapshot for a CC pair in the inset of Figure 3c and example energy and force binding curves are shown in Figure S8 of the Supporting Information. We note in passing that often the decay exponents for the computed binding curves deviate from the ideal values, although the general trend of faster decay when moving from CC to AA dimers is preserved. Even though this dataset is very similar to that used in Refs. 34, 35, we perform an experiment geared more explicitly towards probing the ability of LR models to capture the tails of different types of interactions. We split the structures into train and test sets based on a threshold separation distance r_{train} measured from the shortest separation r_0 , i.e. we train on shorter-range information and assess whether the model can extrapolate the asymptotic decay. In addition, we include the dissociated limit of vanishing interaction energy, where the supercell contains only one monomer. This setup is consistent with typical scenarios, in which one would like to train the ML models on small simulation cells and use them on larger structures which are inaccessible to fully quantum mechanical methods due to the high computational cost.

As a first experiment, we fit each dimer class separately, using linear models based on a multiscale power spectrum[35] that consists of suitable rotationally invariant products combining both SR descriptors and LODE using a single exponent in the range $p = 1, 2, \dots, 9$. The linear model details and fitting procedures are discussed further in section S6D of the Supporting Information. We analyze the performance of the resulting models in Figure 3, for a training threshold $r_{\text{train}} = 4 \text{ \AA}$. The qualitative observations for other threshold distances, shown in the Supporting Information (Figure S10) are similar. Figure 3a shows the test-set energy RMSE as a function of the model’s potential exponent p for each class of dimers, using an optimized radial basis for $l_{\text{max}} = 1$. In all cases, SR models show poor performance, while the LODE models with appropriate exponents can lead to dramatic improvements by up to an order of magnitude. For example, for the CC pairs we find the best model for $p = 1$, while $p = 6$ perform best for the AA pairs. The optimal values roughly correspond to the ideal exponents for each dimer class. The fact that the variation is somewhat smooth can be understood based on the fact that (1) the model potential is built as a superposition of atomic contributions. Over a finite distance interval, any $1/r^p$ potential can be fitted reasonably well with a superposition of multiple $1/\|\mathbf{r} - \mathbf{r}_i\|^{p'}$ potentials with origins shifted to the atomic positions, even if the exponents $p \neq p'$ do not agree (see section S7 in the in the Supporting Information for a more in-depth discussion); (2) binding curves for real molecules do not exactly match the ideal behavior; (3) interactions with $p > 1$ require more than a single monomial basis. Indeed, considering multiple monomial basis functions ($n_{\text{max}} = 6$, $l_{\text{max}} = 4$) changes the performance curves (Figure 3b). There is a large improvement for dimer classes with a large p (which is consistent with significant contributions

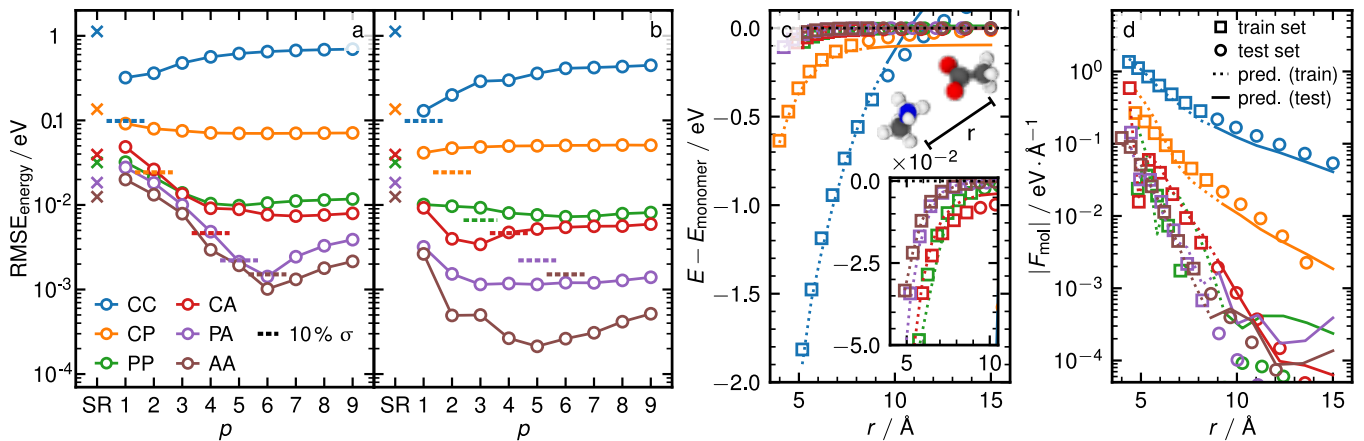


Figure 3. (a) Energy RMSE for models using a single monomial basis as a function of the potential exponent p for the six different dimer classes. Lines between the open circles serve as a guide to the eye. The dashed horizontal lines indicate 10% of the standard deviation σ of the training energies for each subset, which indicates the energy scale of each type of interactions. All lines are color-coded based on the type of dimers, as indicated in the legend. (b) Same as in panel (a) but using multiple radial basis functions ($n_{\max} = 6, l_{\max} = 4$). (c) Binding energies $E - E_{\text{monomer}}$ as a function of the distance r . Open squares show data taken for the train set while open circles show data from the test set. Lines show the predictions of the model. For each dimer class, the exponent p with the highest prediction accuracy in panel (b) is used. The representative dimer is chosen such that its prediction errors are closest to the average behavior. The inset shows a snapshot of a positively charged methylamine and negatively charged acetate at a center of mass distance of $r_0 = 4.6$ Å. (d) Molecular force $|F_{\text{mol}}|$ of the first molecule as a function of the distance r . Symbols and curves are chosen in the same manner as in panel (c).

from several monomial coefficients), but also for $p = 1$. The dependency of the accuracy on the LODE exponent is also less sharp, which is consistent with our theoretical analysis, that shows that higher- l basis functions lead to terms that decay as $1/r^{p+l}$. It should be noted that for the best exponents, the results are best for the AA and PA subsets, which is in part due to the larger size of the training set (around sixfold for AA compared to CC). In addition, the training is done on the total energy and forces, which also include SR terms and prove difficult to fit with this data set that is entirely focused on long-range contributions. This comparison underscores a key observation in this work: LR interactions in realistic systems cannot be fully captured by the idealized asymptotics. Still, LODE features with an exponent adapted to the dimer class usually *do* perform better, which testifies to the added value of using a physically-interpretable framework.

Given the ability of LODE features to target different types of interactions, it is interesting to investigate a model trained against the entire dataset. This is particularly challenging because of the vastly different energy scale of the interactions, which is apparent in Figure 3, and because it is more difficult for the model to infer the correct asymptotic behavior of the interactions based on SR training data. A linear model based only on $p = 1$ coefficients yields respectable performance for all dimer classes *separately*, but when applied to the full dataset the errors increase by an order of magnitude or more (Figure 4). When compared with the intrinsic energy scale, results are particularly poor for the faster-decaying interactions that are completely overshadowed by the

much stronger variability in the CC binding curves: in terms of absolute errors, the error on the LR part for PP, PA, AA dimers is comparable to that on the CC subset.

The overwhelming dominance of strong interactions cannot be addressed by using more flexible models that include multiple exponents, nor by adding a non-linear layer on top of the LODE features (Figure 4, light orange and green bars). A more effective strategy, instead, is to reduce the variability in energy scale by restricting the model to the dimer types that do not contain charged residues (Figure 4, red bars). This reduces the errors on PP, PA and AA dimers by an order of magnitude. Larger training sets might allow to increase the accuracy when targeting all types of non-bonded interactions. However, our computational experiment highlights one of the inherent challenges when extending ML potential to LR physics. Without including ad hoc structures, and designing training targets that single out the desired type of contributions, fitting models on total energy and forces focuses on the larger, SR or electrostatic terms. Other non-bonded interactions that are important to drive collective effects, but small in absolute magnitude, risk being completely neglected even with a model based on physically-inspired terms.

Summarizing our results, we present an extension of the long-distance equivariant framework to arbitrary potential exponents, and give a direct physical interpretation of the LODE coefficients. We prove a direct link between LODE features and the multipole expansion – which we use to propose a physically-motivated radial basis which is adapted to the modeling of the far-field contributions – and show that combining LODE coefficients

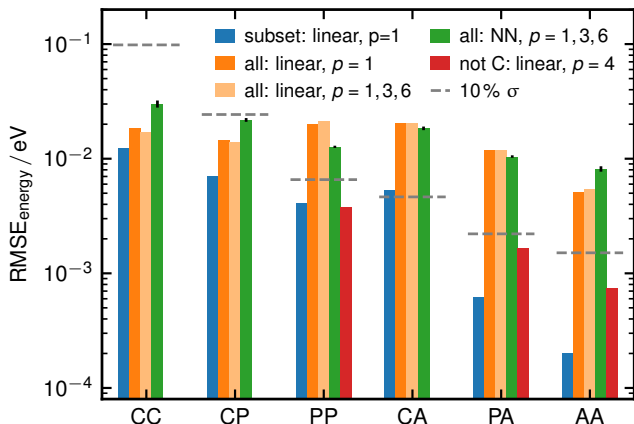


Figure 4. Energy RMSEs for the different subsets of the dimers. Blue bars show the RMSEs of models using a single $p = 1$ LODE exponent similar to Figure 3a, but fitted only on energies. Orange and light orange bars show linear models fit to the whole dataset, either only using $p = 1$ or combining $p = 1, 3, 6$ for the features. Green bars show a fit to the whole dataset with a non-linear neural network model, again with features combining $p = 1, 3, 6$. Red bars correspond to a linear model restricted to non-charged fragments, using $p = 4$ (see section S6D of the Supporting Information). Horizontal gray lines depict a relative error of $10\% \sigma$ for each subset.

in a way analogous to what is done with atom-centered density correlations provides a systematic way to express many-body long-range physics. We also provide a fast and modular implementation of this framework using the GTO as well as an optimized radial basis, which also includes calculations of gradients, making it possible to train on forces. This physically-interpretable yet generally-applicable class of descriptors allows us to investigate the challenges inherent in the ML modeling of LR interactions, revealing the delicate balance between physical content and generality of a model. While it is beneficial to use descriptors that are designed to reflect the expected asymptotic decay of the interactions, we observe that in a realistic application doing so is neither strictly necessary, nor a guarantee of success. LODE-based models can reach levels of accuracy of a small fraction of the typical binding energy for different types of asymptotic behavior, but only when separately targeting

chemically homogeneous sets of molecules. When considering a heterogeneous dataset that contains very different kinds of intermolecular interactions, the large variability in the energy scale of the different physical terms makes it particularly difficult to achieve good relative accuracy for the weaker types of interactions. The description of LR interactions, from the bare interactions themselves to more complex processes such as nonlocal charge transfers, remains one of the key challenges to the application of ML techniques to atomistic simulations. The extension of the LODE framework we introduce here provides a flexible, physically-motivated solution, and a sandbox to investigate the effects of descriptor engineering and ML architecture, balancing interpretability and generality of the model.

ACKNOWLEDGEMENTS

The Authors acknowledge funding from the European Research Council (ERC) under the European Union’s Horizon 2020 research and innovation programme (grant agreement No 101001890-FIAMMA). We would like to thank Guillaume Fraux and all the members of the Laboratory of Computational Science and Modeling for their contributions to the software infrastructure that enabled this study. We also thank Andrea Grisafi and Jigyasa Nigam for insightful discussion.

SUPPORTING MATERIAL

The electronic supporting material for this publication include a pedagogic derivation of the connection between generalized LODE features and the multipole expansion, further details on the different models and datasets, and the dimer dataset used for the benchmarks. All used datasets as well as the input for the DFT calculations are available for download at <https://doi.org/10.24435/materialscloud:23-99>. Generalized LODE descriptors can be computed using the *rascaline* package, available at <https://github.com/luthaf/rascaline>. Additional source codes for constructing the monomial basis in *rascaline* as well as the code to train the linear and the neural networks are available on zenodo <https://doi.org/10.5281/zenodo.8399545>

[1] Behler, J.; Parrinello, M. Generalized Neural-Network Representation of High-Dimensional Potential-Energy Surfaces. *Phys. Rev. Lett.* **2007**, *98*, 146401.
 [2] Bartók, A. P.; Payne, M. C.; Kondor, R.; Csányi, G. Gaussian Approximation Potentials: The Accuracy of Quantum Mechanics, without the Electrons. *Phys. Rev. Lett.* **2010**, *104*, 136403.

[3] Bartók, A. P.; Kondor, R.; Csányi, G. On Representing Chemical Environments. *Phys. Rev. B* **2013**, *87*, 184115.
 [4] Musil, F.; Grisafi, A.; Bartók, A. P.; Ortner, C.; Csányi, G.; Ceriotti, M. Physics-Inspired Structural Representations for Molecules and Materials. *Chem. Rev.* **2021**, *121*, 9759–9815.
 [5] Rupp, M.; Tkatchenko, A.; Müller, K.-R.; von Lilienfeld, O. A. Fast and Accurate Modeling of Molecular At-

- omization Energies with Machine Learning. *Phys. Rev. Lett.* **2012**, *108*, 058301.
- [6] Glielmo, A.; Sollich, P.; De Vita, A. Accurate Interatomic Force Fields via Machine Learning with Covariant Kernels. *Phys. Rev. B* **2017**, *95*, 214302.
- [7] Grisafi, A.; Wilkins, D. M.; Csányi, G.; Ceriotti, M. Symmetry-Adapted Machine Learning for Tensorial Properties of Atomistic Systems. *Phys. Rev. Lett.* **2018**, *120*, 036002.
- [8] Wilkins, D. M.; Grisafi, A.; Yang, Y.; Lao, K. U.; DiStasio, R. A.; Ceriotti, M. Accurate Molecular Polarizabilities with Coupled Cluster Theory and Machine Learning. *PNAS* **2019**, *116*, 3401–3406.
- [9] Brockherde, F.; Vogt, L.; Li, L.; Tuckerman, M. E.; Burke, K.; Müller, K. R. Bypassing the Kohn-Sham Equations with Machine Learning. *Nat. Commun.* **2017**, *8*, 872.
- [10] Alred, J. M.; Bets, K. V.; Xie, Y.; Yakobson, B. I. Machine Learning Electron Density in Sulfur Crosslinked Carbon Nanotubes. *Composites Science and Technology* **2018**, *166*, 3–9.
- [11] Fabrizio, A.; Grisafi, A.; Meyer, B.; Ceriotti, M.; Corminboeuf, C. Electron Density Learning of Non-Covalent Systems. *Chemical Science* **2019**, *10*, 9424–9432.
- [12] Lewis, A. M.; Grisafi, A.; Ceriotti, M.; Rossi, M. Learning Electron Densities in the Condensed Phase. *J. Chem. Theory Comput.* **2021**, *17*, 7203–7214.
- [13] Schütt, K. T.; Gastegger, M.; Tkatchenko, A.; Müller, K.-R.; Maurer, R. J. Unifying Machine Learning and Quantum Chemistry with a Deep Neural Network for Molecular Wavefunctions. *Nat Commun* **2019**, *10*, 5024.
- [14] Nigam, J.; Willatt, M. J.; Ceriotti, M. Equivariant Representations for Molecular Hamiltonians and N-center Atomic-Scale Properties. *J. Chem. Phys.* **2022**, *156*, 014115.
- [15] Carleo, G.; Troyer, M. Solving the Quantum Many-Body Problem with Artificial Neural Networks. *Science* **2017**, *355*, 602–606.
- [16] Hermann, J.; Schätzle, Z.; Noé, F. Deep-Neural-Network Solution of the Electronic Schrödinger Equation. *Nat. Chem.* **2020**, *12*, 891–897.
- [17] Kohn, W. Density Functional and Density Matrix Method Scaling Linearly with the Number of Atoms. *Phys. Rev. Lett.* **1996**, *76*, 3168–3171.
- [18] Prodan, E.; Kohn, W. Nearsightedness of Electronic Matter. *Proceedings of the National Academy of Sciences* **2005**, *102*, 11635–11638.
- [19] Ambrosetti, A.; Ferri, N.; DiStasio, R. A.; Tkatchenko, A. Wavelike Charge Density Fluctuations and van Der Waals Interactions at the Nanoscale. *Science* **2016**, *351*, 1171–1176.
- [20] Jackson, J. D. *Classical Electrodynamics Third Edition*, 3rd ed.; Wiley: New York, 1998.
- [21] Israelachvili, J. N. *Intermolecular and Surface Forces (Third Edition)*, third edition ed.; Academic Press: San Diego, 2011.
- [22] Kanduć, M.; Schneck, E.; Netz, R. R. Attraction between Hydrated Hydrophilic Surfaces. *Chemical Physics Letters* **2014**, *610–611*, 375–380.
- [23] Hansen, J.-P., McDonald, I. R., Eds. *Theory of Simple Liquids (Fourth Edition)*; Academic Press: Oxford, 2013; p i.
- [24] Deng, Z.; Chen, C.; Li, X.-G.; Ong, S. P. An Electrostatic Spectral Neighbor Analysis Potential for Lithium Nitride. *npj Computational Materials* **2019**, *5*, 1–8.
- [25] Deringer, V. L.; Caro, M. A.; Csányi, G. A General-Purpose Machine-Learning Force Field for Bulk and Nanostructured Phosphorus. *Nat Commun* **2020**, *11*, 5461.
- [26] Niblett, S. P.; Galib, M.; Limmer, D. T. Learning Intermolecular Forces at Liquid–Vapor Interfaces. *J. Chem. Phys.* **2021**, *155*, 164101.
- [27] Peng, Y.; Lin, L.; Ying, L.; Zepeda-Núñez, L. Efficient Long-Range Convolutions for Point Clouds. *Journal of Computational Physics* **2023**, *473*, 111692.
- [28] Zhang, L.; Wang, H.; Muniz, M. C.; Panagiotopoulos, A. Z.; Car, R.; E, W. A Deep Potential Model with Long-Range Electrostatic Interactions. *J. Chem. Phys.* **2022**, *156*, 124107.
- [29] Faraji, S.; Ghasemi, S. A.; Rostami, S.; Rasoulkhani, R.; Schaefer, B.; Goedecker, S.; Amsler, M. High Accuracy and Transferability of a Neural Network Potential through Charge Equilibration for Calcium Fluoride. *Phys. Rev. B* **2017**, *95*, 104105.
- [30] Ko, T. W.; Finkler, J. A.; Goedecker, S.; Behler, J. A Fourth-Generation High-Dimensional Neural Network Potential with Accurate Electrostatics Including Non-Local Charge Transfer. *Nat Commun* **2021**, *12*, 398.
- [31] Ko, T. W.; Finkler, J. A.; Goedecker, S.; Behler, J. General-Purpose Machine Learning Potentials Capturing Nonlocal Charge Transfer. *Acc. Chem. Res.* **2021**, *54*, 808–817.
- [32] Gao, A.; Remsing, R. C. Self-Consistent Determination of Long-Range Electrostatics in Neural Network Potentials. *Nat Commun* **2022**, *13*, 1572.
- [33] Anstine, D. M.; Isayev, O. Machine Learning Interatomic Potentials and Long-Range Physics. *J. Chem. Phys.* **2023**, *127*, 2417–2431.
- [34] Grisafi, A.; Ceriotti, M. Incorporating Long-Range Physics in Atomic-Scale Machine Learning. *J. Chem. Phys.* **2019**, *151*, 204105.
- [35] Grisafi, A.; Nigam, J.; Ceriotti, M. Multi-Scale Approach for the Prediction of Atomic Scale Properties. *Chem. Sci.* **2021**, *12*, 2078–2090.
- [36] Grisafi, A.; Ceriotti, M. Incorporating Long-Range Physics in Atomic-Scale Machine Learning. *J. Chem. Phys.* **2019**, *151*, 204105.
- [37] Grisafi, A.; Nigam, J.; Ceriotti, M. Multi-Scale Approach for the Prediction of Atomic Scale Properties. *Chem. Sci.* **2021**, *12*, 2078–2090.
- [38] Nijboer, B. R. A.; De Wette, F. W. On the Calculation of Lattice Sums. *Physica* **1957**, *23*, 309–321.
- [39] Willatt, M. J.; Musil, F.; Ceriotti, M. Atom-Density Representations for Machine Learning. *J. Chem. Phys.* **2019**, *150*, 154110.
- [40] Drautz, R. Atomic Cluster Expansion for Accurate and Transferable Interatomic Potentials. *Phys. Rev. B* **2019**, *99*, 014104.
- [41] Williams, D. E. Accelerated Convergence of Crystal-Lattice Potential Sums. *Acta Crystallographica Section A: Crystal Physics, Diffraction, Theoretical and General Crystallography* **1971**, *27*, 452–455.
- [42] Williams, D. E. Accelerated Convergence Treatment of R-n Lattice Sums. *Crystallography Reviews* **1989**, *2*, 3–23.
- [43] Nigam, J.; Pozdnyakov, S.; Ceriotti, M. Recursive Evaluation and Iterative Contraction of N -Body Equivariant Features. *J. Chem. Phys.* **2020**, *153*, 121101.

- [44] Darden, T.; York, D.; Pedersen, L. Particle Mesh Ewald: An $N \cdot \log(N)$ Method for Ewald Sums in Large Systems. *J. Chem. Phys.* **1993**, *98*, 10089–10092.
- [45] Essmann, U.; Perera, L.; Berkowitz, M. L.; Darden, T.; Lee, H.; Pedersen, L. G. A Smooth Particle Mesh Ewald Method. *J. Chem. Phys.* **1995**, *103*, 8577–8593.
- [46] Eastwood, R. W. H., J. W. *Computer Simulation Using Particles*; CRC Press, 1988.
- [47] Frenkel, D.; Smit, B. *Understanding Molecular Simulation: From Algorithms to Applications*, 2nd ed.; Computational Science Series 1; Academic Press: San Diego, 2002.
- [48] Burns, L. A.; Faver, J. C.; Zheng, Z.; Marshall, M. S.; Smith, D. G. A.; Vanommeslaeghe, K.; MacKerell, A. D.; Merz, K. M.; Sherrill, C. D. The BioFragment Database (BFDdb): An Open-Data Platform for Computational Chemistry Analysis of Noncovalent Interactions. *J. Chem. Phys.* **2017**, *147*, 161727.
- [49] Heyd, J.; Scuseria, G. E.; Ernzerhof, M. Hybrid Functionals Based on a Screened Coulomb Potential. *J. Chem. Phys.* **2003**, *118*, 8207–8215.
- [50] Hermann, J.; Tkatchenko, A. Density Functional Model for van Der Waals Interactions: Unifying Many-Body Atomic Approaches with Nonlocal Functionals. *Phys. Rev. Lett.* **2020**, *124*, 146401.

Physics-inspired Equivariant Descriptors of Non-bonded Interactions

Supporting Information

Kevin K. Huguenin-Dumittan,^{1,*} Philip Loche,^{1,*} Ni Haoran,¹ and Michele Ceriotti^{1,†}

¹Laboratory of Computational Science and Modeling, IMX,
École Polytechnique Fédérale de Lausanne, 1015 Lausanne, Switzerland

CONTENTS

S1	Multipole Expansion: Review and Extension	S2
A	Overview	S2
B	Multipole Expansion for Coulomb Potential	S3
1.	Key ingredient: Laplace Expansion of Coulomb Potential	S3
2.	Interior Charges	S5
3.	Exterior Charges	S6
4.	Inter-Regional Interaction Energy	S7
C	Extension of Multipole Expansion to General Inverse Power-Law Potential	S7
1.	Key ingredient: Laplace Expansion of General Power-Law Potential	S7
2.	Interior Charges	S9
3.	Exterior Charges	S10
4.	Inter-Regional Interaction Energy	S10
D	Remark On Conventions and Prefactors	S11
S2	Physical Interpretation and Optimization of LODE Representation	S11
A	Overview of this section	S11
B	General Framework for Atomic Representations	S11
C	LODE for Coulombic Interactions	S12
D	Extension to Arbitrary Long-Range Descriptors	S13
E	Physical Interpretation and Optimizations for the Coulombic Case	S14
F	Physical Interpretation and Optimizations for General Exponents	S15
G	Building ML Models	S16
H	Similarities and Differences of the LODE Density with the actual Coulomb Potential	S17
1.	Absence of SR-LR splitting	S17
2.	Treatment of different chemical species	S17
S3	Behavior of General Density Contribution Function	S18
A	Long-Range Limit	S19
B	Short-Range Limit	S19
C	Coulombic Special Case	S19
D	Why Gaussian Densities cannot be used in the general case	S20
S4	Higher Order Descriptors and Many-Body Effects	S20
A	Review of Invariant Descriptors	S20
B	Interpretation of LODE coefficients in Terms of Many-Body Interactions	S21
C	Results on Many-Body Dispersion	S22
1.	Fitting DFT Data	S22
2.	Model Details	S22
3.	Fitting the ATM Potential	S23
S5	Model Details for the Point-Charge Toy problem	S24
S6	Computational details for the Dimer Dataset	S25
A	Reference energy calculations	S26
B	Empirical interaction exponents	S26
C	SOAP and LODE Hyperparameters	S26
D	Linear Models: Separate Dimer Classes	S28
E	Atomic Force Errors	S28

* Contributed equally to this work

† michele.ceriotti@epfl.ch

F Test Errors for Different Training Cutoffs	S28
G Energy Errors for Combined Linear Models Using Non-Charged Fragments	S30
H Details of the Neural Network Models	S30
I Relative Energy Errors for Different Subsets	S31
S7 Flexibility of power-law fits	S31
References	S33

S1. MULTIPOLE EXPANSION: REVIEW AND EXTENSION

A. Overview

A key ingredient for our analysis is the multipole expansion from electrostatics. To summarize the general idea, let $\rho(\mathbf{r})$ be some density function that decays sufficiently fast as $r \rightarrow \infty$, in a sense that will be made more precise later on.

As shown in Figure S1a, we split the density up into an interior part $\rho^<$ and exterior part $\rho^>$, each containing only the density inside / outside the cutoff radius r_{cut} , respectively. More formally, this can be written as

$$\rho^<(\mathbf{r}) = \begin{cases} \rho(\mathbf{r}) & r < r_{\text{cut}} \\ 0 & r \geq r_{\text{cut}} \end{cases}, \quad \rho^>(\mathbf{r}) = \begin{cases} 0 & r < r_{\text{cut}} \\ \rho(\mathbf{r}) & r \geq r_{\text{cut}} \end{cases}, \quad (\text{S1})$$

where $r = |\mathbf{r}|$ and $r' = \|\mathbf{r}'\|$. For the rest of this document, we shall denote by \mathbf{r} (\mathbf{r}') a point inside (outside) the cutoff, meaning that we will always have $r < r_{\text{cut}}$ ($r' > r_{\text{cut}}$). In particular, $r < r'$ will always be true.

We begin by providing a general overview of the multipole expansion: Now that we have divided space into two regions (interior and exterior), the multipole expansion is a technique that can be used to study the potential generated by charges in one region evaluated in the other region. To be more specific, we will derive expressions for the following three quantities:

1. The ‘‘famous version’’: The ‘‘electrostatic’’ potential $V^<$ generated by the interior charges, evaluated at a point \mathbf{r}' in the exterior region as shown in Figure S1b and explicitly given by

$$V^<(\mathbf{r}') = \int_0^{r_{\text{cut}}} d^3\mathbf{r} \frac{\rho^<(\mathbf{r})}{\|\mathbf{r} - \mathbf{r}'\|^p}, \quad (\text{S2})$$

where the integral runs over the entire interior region with $r < r_{\text{cut}}$.

2. The opposite of the above, i.e. the potential $V^>$ generated by the exterior charges, evaluated at a point \mathbf{r} in the interior region as shown in Figure S1c and explicitly given by

$$V^>(\mathbf{r}) = \int_{r_{\text{cut}}}^{\infty} d^3\mathbf{r}' \frac{\rho^>(\mathbf{r}')}{\|\mathbf{r} - \mathbf{r}'\|^p}, \quad (\text{S3})$$

where the integral runs over the entire exterior region with $r' > r_{\text{cut}}$.

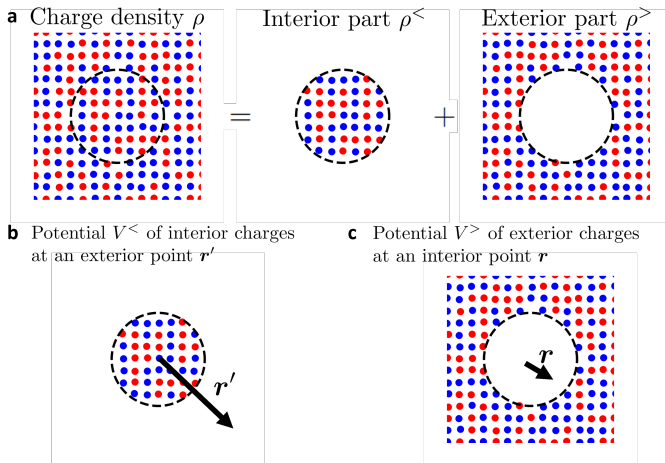


Figure S1. Visual representation of the various versions of the multipole expansion: a shows the splitting of a charge density into an interior and exterior part. b shows the ‘‘famous version’’ of the multipole expansion discussion in point 1. c shows the converse, in which the charges are outside and the potential is evaluated in the interior region.

3. The “electrostatic” interaction energy between the two regions: it consists of interaction terms of the form $\frac{q_i q_j}{\|\mathbf{r}_i - \mathbf{r}'_j\|^p}$, where particle i is from the interior and j from the exterior region. In other words, it includes the inter-regional interactions but not the intra-regional ones. For the continuous charge densities treated here, this can be written as

$$E_{\text{int}} = \int_0^{r_{\text{cut}}} d^3 \mathbf{r} \int_{r_{\text{cut}}}^{\infty} d^3 \mathbf{r}' \frac{\rho^<(\mathbf{r}) \rho^>(\mathbf{r}')}{\|\mathbf{r} - \mathbf{r}'\|^p}. \quad (\text{S4})$$

The multipole expansion essentially provides a mathematically elegant way to express the three quantities defined in Equation (S2), (S3) and (S4).

The separation into the two regions might at first seem arbitrary, but turns out to be a key ingredient: In Equation (S2), for instance, we can observe that for the entire region of integration, we always have $r < r'$ since \mathbf{r}' was specifically chosen to be a point in the exterior region $r' > r_{\text{cut}}$. This inequality will be essential to obtain a simple mathematical expression for the end result.

The most famous version of the multipole expansion that is discussed in many graduate level textbooks on electrodynamics deals with the first case, in which the charges are confined to some interior region,¹ and is restricted to the Coulomb potential for which $p = 1$. The same derivation with tiny modifications also lead to the analogous results for the second (Equation (S3)) and third (Equation (S4)) cases. In fact, the proofs for all cases are quite simple once one knows one key intermediate result that is common to all three versions: the Laplace expansion of the Coulomb potential. A unified description of these for the Coulomb potential is discussed in [section S1 B](#).

As part of this work, the multipole expansion was extended to arbitrary exponents p . The general case turns out to be more complicated than the Coulomb special case, the underlying reason being the fact that the Coulomb potential is a solution to the Laplace equation $\Delta \frac{1}{r} = 0$ for $r \neq 0$. This can be seen most directly by performing the multipole expansion in Cartesian coordinates. The analogous results for general exponents p are discussed in [section S1 C](#).

B. Multipole Expansion for Coulomb Potential

1. Key ingredient: Laplace Expansion of Coulomb Potential

All variants of the multipole expansion are quite simple to derive once we understand a single key ingredient: the Laplace expansion of the Coulomb potential. In this subsection, we will first state the result and provide some intuition for why it is such an essential tool. For the more mathematically inclined readers, this is then followed by a sketch of the proof, but readers may feel free to skip this part and move on to the following subsections in which the Laplace expansion is used to derive the various versions of the multipole expansion.

Lemma S1.1 (Laplace Expansion of Coulomb Potential). *Let $\mathbf{r}, \mathbf{r}' \in \mathbb{R}^3$ such that $r < r'$. Then,*

$$\frac{1}{\|\mathbf{r} - \mathbf{r}'\|} = \sum_{l,m} \frac{4\pi}{2l+1} \frac{r^l}{r'^{l+1}} Y_l^m(\hat{\mathbf{r}}') Y_l^m(\hat{\mathbf{r}}), \quad (\text{S5})$$

where $\sum_{l,m}$ is a shorthand for $\sum_{l=0}^{\infty} \sum_{m=-l}^l$ and the functions Y_l^m are the real spherical harmonics.

The key idea is that we have managed to rewrite the the original expression, which depends on both \mathbf{r} and \mathbf{r}' , into a form in which the two variables are separated, namely:

$$\frac{1}{\|\mathbf{r} - \mathbf{r}'\|} = \sum_{l,m} \frac{4\pi}{2l+1} \cdot \underbrace{\frac{1}{r'^{l+1}} Y_l^m(\hat{\mathbf{r}}')}_{\text{only depends on } \mathbf{r}'} \cdot \underbrace{r^l Y_l^m(\hat{\mathbf{r}})}_{\text{only depends on } \mathbf{r}}. \quad (\text{S6})$$

The radial dependencies (the factors of r^l and $1/r'^{l+1}$) also explain why we need to split the charges into an interior and exterior part when we later discuss the full multipole expansion. For two general vectors \mathbf{r}_1 and \mathbf{r}_2 , the Laplace expansion of $1/\|\mathbf{r}_1 - \mathbf{r}_2\|$ would contain factors of r_{\min}^l and $1/r_{\max}^{l+1}$, where r_{\max} (r_{\min}) is the larger (smaller) of the two radii r_1 and r_2 . By dividing the charges into an interior and exterior region, we will always have $r < r'$ and thus $r_{\min} = r$, $r_{\max} = r'$. Otherwise, one would need to mix factors of $\frac{r^l}{r'^{l+1}}$ and $\frac{r'^l}{r^{l+1}}$, leading to significantly more complicated final expressions.

For readers not as familiar with the *real* spherical harmonics, these are essentially the same functions as the complex counterparts more often encountered in the mathematical literature. They are analogous to solutions of the differential

equation $f'' = -f$, two commonly used forms being $f(x) = Ae^{ix} + Be^{-ix}$ or $f(x) = C \cos x + D \sin x$. The complex spherical harmonics correspond to the exponential solutions $e^{\pm ix}$, and tend to be easier to work with in proofs, while the trigonometric functions are real-valued, and hence favorable in applications in which the target function f is known to be real. For this reason and for simpler notation, we use the real form, but all results would remain essentially the same with complex spherical harmonics, the only difference being that half of the spherical harmonics would need to be replaced by their complex conjugate.

We devote the rest of this subsection to the proof of the Laplace expansion. It is not required to understand this proof to get to the multipole expansion in the next subsection.

Proof. The proof consists of three steps. The first one only requires relatively elementary algebra, while the other two will require some knowledge about special functions (Legendre polynomials and spherical harmonics). We begin by writing the left hand side explicitly in terms of the moduli r, r' as well as the angle γ between the vectors \mathbf{r} and \mathbf{r}' ,

$$\frac{1}{\|\mathbf{r} - \mathbf{r}'\|} = \frac{1}{((\mathbf{r} - \mathbf{r}')^2)^{\frac{1}{2}}} = \frac{1}{(r^2 + r'^2 - 2rr' \cos \gamma)^{\frac{1}{2}}} = \frac{1}{r' \left(\left(\frac{r}{r'}\right)^2 + 1 - 2 \left(\frac{r}{r'}\right) \cos \gamma \right)^{\frac{1}{2}}}, \quad (\text{S7})$$

where we pulled out a factor of r' in the last step, and the angular part can be explicitly computed as $\cos \gamma = \hat{\mathbf{r}} \cdot \hat{\mathbf{r}}'$.

For the second step, we use an identity involving Legendre polynomials in terms of a generating function, namely

$$\frac{1}{(1 - 2cx + x^2)^{\frac{1}{2}}} = \sum_{l=0}^{\infty} P_l(c)x^l \quad (\text{S8})$$

for any $x, c \in \mathbb{R}$ with $|c| < 1$ and $|x| < 1$. In fact, this equation can be used to define the Legendre polynomials in the first place. We can use this identity with $x = r/r'$ and $c = \cos \gamma = \hat{\mathbf{r}} \cdot \hat{\mathbf{r}}'$, which leads us to

$$\frac{1}{\|\mathbf{r} - \mathbf{r}'\|} = \frac{1}{r'} \frac{1}{\left(1 - 2 \left(\frac{r}{r'}\right) (\hat{\mathbf{r}} \cdot \hat{\mathbf{r}}') + \left(\frac{r}{r'}\right)^2\right)^{\frac{1}{2}}} \quad (\text{S9})$$

$$= \frac{1}{r'} \sum_{l=0}^{\infty} P_l(\hat{\mathbf{r}} \cdot \hat{\mathbf{r}}') \frac{r^l}{r'^l} = \sum_{l=0}^{\infty} P_l(\hat{\mathbf{r}} \cdot \hat{\mathbf{r}}') \frac{r^l}{r'^{l+1}}. \quad (\text{S10})$$

Note that at this point, we have managed to separate the radial dependences with respect to r and r' , but not yet the angular part.

Thus, for the third and final step, we will use the spherical harmonics addition theorem, which connects the spherical harmonics to the Legendre polynomials:

$$P_l(\hat{\mathbf{r}} \cdot \hat{\mathbf{r}}') = \sum_{m=-l}^l \frac{4\pi}{2l+1} Y_l^m(\hat{\mathbf{r}}') Y_l^m(\hat{\mathbf{r}}) \quad (\text{S11})$$

for any two unit vectors $\hat{\mathbf{r}}$ and $\hat{\mathbf{r}}'$. Note that this theorem is typically derived using the complex form of the spherical harmonics, in which case the first spherical harmonic is replaced by the complex conjugate. Extending this theorem to real spherical harmonics is then straight-forward using the fact that the conversion between real and complex spherical harmonics is a unitary transformation.

With this step, we have now separated the angular dependence with respect to $\hat{\mathbf{r}}$ and $\hat{\mathbf{r}}'$. Using this, we finally obtain the desired result

$$\frac{1}{\|\mathbf{r} - \mathbf{r}'\|} = \sum_{l,m} \frac{4\pi}{2l+1} \frac{r^l}{r'^{l+1}} Y_l^m(\hat{\mathbf{r}}') Y_l^m(\hat{\mathbf{r}}). \quad (\text{S12})$$

For completeness, the analogous result with complex spherical harmonics would be

$$\frac{1}{\|\mathbf{r} - \mathbf{r}'\|} = \sum_{l,m} \frac{4\pi}{2l+1} \frac{r^l}{r'^{l+1}} Y_{\text{complex},l}^{*m}(\hat{\mathbf{r}}') Y_{\text{complex},l}^m(\hat{\mathbf{r}}). \quad (\text{S13})$$

□

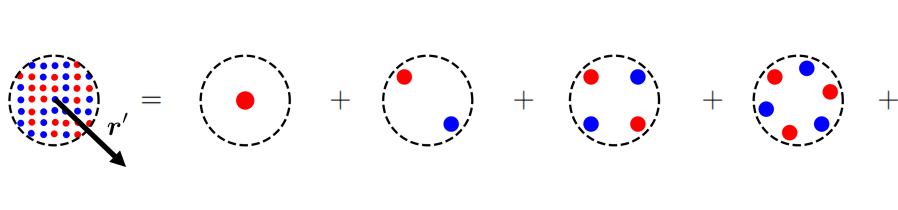


Figure S2. Visual representation of the interior multipole expansion. The potential generated by the interior charges can be decomposed into terms of increasing angular frequencies here illustrated for the first four ($l = 0, 1, 2, 3$) terms.

2. Interior Charges

We have now completed the most challenging part of the derivation, and are well-prepared to easily prove the multipole expansion theorems for the Coulomb potential. We begin by discussing the most well-known version of the Coulomb potential, which is discussed in many textbooks on electrodynamics¹ and is illustrated in [Figure S2](#).

Theorem S1.2. *Let $\rho^<$ be a localized charge density which is entirely contained within a cutoff radius r_{cut} . The resulting electrostatic potential $V^<(\mathbf{r}')$ evaluated at some point \mathbf{r}' outside of the cutoff is given by*

$$V^<(\mathbf{r}') = \sum_{lm} M_{lm}^< \frac{1}{r'^{l+1}} Y_l^m(\hat{\mathbf{r}}'), \quad (\text{S14})$$

with coefficients

$$M_{lm}^< = \frac{4\pi}{2l+1} \int_0^{r_{\text{cut}}} d^3\mathbf{r} r^l Y_l^m(\hat{\mathbf{r}}) \rho^<(\mathbf{r}). \quad (\text{S15})$$

The coefficients M_{lm} are called **(interior) multipole moments** and completely characterize the potential in the exterior region. The first term with $l = 0$ is called the monopole term and generates a spherically symmetric potential decaying as $1/r$. The prefactor $M_{00}^<$ simply corresponds to the total charge. The second term with $l = 1$ is called the dipole term and generates a potential decaying as $1/r^2$. It represents the first correction to the spherically symmetrical approximation. More generally, as shown in [Figure S2](#), the multipole expansion can be thought of as a Fourier-like expansion of $\rho^<$ into angular frequency components. The term with an angular frequency l leads to a potential decaying as $1/r^{1+l}$, showing that terms with high l become less and less important as $r \rightarrow \infty$.

Proof. From the superposition principle, the electrostatic potential generated by $\rho^<$ is given by

$$V^<(\mathbf{r}') = \int_0^{r_{\text{cut}}} d^3\mathbf{r} \frac{\rho^<(\mathbf{r})}{\|\mathbf{r} - \mathbf{r}'\|}. \quad (\text{S16})$$

Since $r' > r_{\text{cut}}$, we have $r < r'$ in the entire domain of integration. This allows us to use the Laplace expansion of the Coulomb potential $\frac{1}{\|\mathbf{r} - \mathbf{r}'\|} = \sum_{l,m} \frac{4\pi}{2l+1} \frac{r^l}{r'^{l+1}} Y_l^m(\hat{\mathbf{r}}) Y_l^m(\hat{\mathbf{r}}')$ (Lemma (S5)) to write

$$V^<(\mathbf{r}') = \int_0^{r_{\text{cut}}} d^3\mathbf{r} \rho^<(\mathbf{r}) \sum_{l,m} \frac{4\pi}{2l+1} \frac{r^l}{r'^{l+1}} Y_l^m(\hat{\mathbf{r}}) Y_l^m(\hat{\mathbf{r}}'). \quad (\text{S17})$$

Assuming that $\rho^<$ is continuous on the entire interior domain (including the boundary), it is permissible to interchange the order of summation and integration from Fubini's theorem, which leads to

$$V^<(\mathbf{r}') = \sum_{l,m} \underbrace{\frac{4\pi}{2l+1} \int_0^{r_{\text{cut}}} d^3\mathbf{r} \rho^<(\mathbf{r}) r^l Y_l^m(\hat{\mathbf{r}})}_{=: M_{lm}^<} \frac{1}{r'^{l+1}} Y_l^m(\hat{\mathbf{r}}') = \sum_{l,m} M_{lm}^< \frac{1}{r'^{l+1}} Y_l^m(\hat{\mathbf{r}}') \quad (\text{S18})$$

with multipole moment

$$M_{lm}^< = \int_0^{r_{\text{cut}}} d^3\mathbf{r} r^l Y_l^m(\hat{\mathbf{r}}) \rho^<(\mathbf{r}). \quad (\text{S19})$$

This is the desired result, in which the exterior potential is written as a series in varying angular and radial dependence. \square

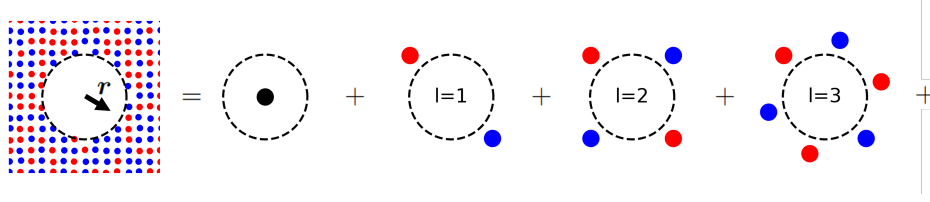


Figure S3. Visual representation of the exterior multipole expansion. The potential generated by the exterior charges can be decomposed into terms of increasing angular frequencies here illustrated for $l = 0, 1, 2, 3$ corresponding to the monopole, dipole, quadrupole and octupole terms.

3. Exterior Charges

We can now flip the roles between the exterior and interior regions: the charges are now outside, and we wish to compute the potential generated by these in the interior region. The result is analogous to the previous case, except that all factors of r^l and $1/r'^l$ switch roles.

Theorem S1.3. *Let $\rho^>$ be a charge density which is entirely contained outside of a cutoff radius r_{cut} . The resulting electrostatic potential $V^>(\mathbf{r})$ evaluated at some point \mathbf{r} inside of the cutoff is given by*

$$V^>(\mathbf{r}) = \sum_{lm} M_{lm}^> r^l Y_l^m(\hat{\mathbf{r}}), \quad (\text{S20})$$

with coefficients

$$M_{lm}^> = \frac{4\pi}{2l+1} \int_{r_{\text{cut}}}^{\infty} d^3\mathbf{r}' \frac{1}{r'^{l+1}} Y_l^m(\hat{\mathbf{r}}') \rho^>(\mathbf{r}'). \quad (\text{S21})$$

The coefficients $M_{lm}^>$ will be called **exterior multipole moments** in this work. As for the interior version, this can be interpreted as a decomposition of the exterior charge density $\rho^>$ into (angular) frequency components as is illustrated in Figure S3.

Proof. The proof follows along the exact same lines as the previous version, except that r and r' switch roles. From the superposition principle, the potential generated by the exterior charges is given by

$$V^>(\mathbf{r}) = \int_{r_{\text{cut}}}^{\infty} d^3\mathbf{r}' \frac{\rho^>(\mathbf{r}')}{\|\mathbf{r} - \mathbf{r}'\|}, \quad (\text{S22})$$

assuming that the charge density $\rho^>$ decays sufficiently quickly for the integral to be well-defined. Using the Laplace expansion of the Coulomb potential (Eq. (S5)), we obtain

$$V^>(\mathbf{r}) = \int_{r_{\text{cut}}}^{\infty} d^3\mathbf{r}' \rho^>(\mathbf{r}') \sum_{l,m} \frac{4\pi}{2l+1} \frac{r^l}{r'^{l+1}} Y_l^m(\hat{\mathbf{r}}') Y_l^m(\hat{\mathbf{r}}). \quad (\text{S23})$$

It is permissible to interchange the order of summation and integration if $\rho^>$ decays sufficiently quickly. Thus,

$$V^>(\mathbf{r}) = \sum_{l,m} \frac{4\pi}{2l+1} \underbrace{\int_{r_{\text{cut}}}^{\infty} d^3\mathbf{r}' \frac{1}{r'^{l+1}} Y_l^m(\hat{\mathbf{r}}') \rho^>(\mathbf{r}') r^l Y_l^m(\hat{\mathbf{r}})}_{=: M_{lm}^>} = \sum_{l,m} M_{lm}^> r^l Y_l^m(\hat{\mathbf{r}}) \quad (\text{S24})$$

with coefficients

$$M_{lm}^> = \frac{4\pi}{2l+1} \int_{r_{\text{cut}}}^{\infty} d^3\mathbf{r}' \frac{1}{r'^{l+1}} Y_l^m(\hat{\mathbf{r}}') \rho^>(\mathbf{r}'). \quad (\text{S25})$$

This is the desired result, in which the interior potential is written as a series in angular and radial dependence. \square

4. Inter-Regional Interaction Energy

We now discuss the third and final useful result that can be derived using the same mathematical methods: the “inter-regional” electrostatic interaction energy E_{int} between the charges in the two regions. More formally, let $\rho^<$ and $\rho^>$ be two charge densities that are confined to the interior / exterior region. The total electrostatic interaction energy E_{int} between the interior and exterior charges (not including the interactions between charges in the same region) is given by

$$E_{\text{int}} = \int_0^{r_{\text{cut}}} d^3\mathbf{r} \int_{r_{\text{cut}}}^{\infty} d^3\mathbf{r}' \frac{\rho^<(\mathbf{r})\rho^>(\mathbf{r}')}{\|\mathbf{r} - \mathbf{r}'\|}. \quad (\text{S26})$$

Obtaining a multipolar expression for this interaction energy will be useful to obtain a physical interpretation of ML models that are built on top of the LODE features.

Theorem S1.4. *The electrostatic interaction energy E_{int} between the interior charges $\rho^<$ and exterior charges $\rho^>$ can be computed as*

$$E_{\text{int}} = \sum_{lm} \frac{2l+1}{4\pi} M_{lm}^> M_{lm}^<, \quad (\text{S27})$$

where $M_{lm}^>$ and $M_{lm}^<$ are the exterior and interior multipole moments defined in the two previous [section S1 B 3](#) and [section S1 B 2](#), respectively.

Proof. The proof should be straight-forward to anyone who has followed the proofs of the two previous versions of the multipole expansion. We start from

$$E_{\text{int}} = \int_0^{r_{\text{cut}}} d^3\mathbf{r} \int_{r_{\text{cut}}}^{\infty} d^3\mathbf{r}' \frac{\rho^<(\mathbf{r})\rho^>(\mathbf{r}')}{\|\mathbf{r} - \mathbf{r}'\|}. \quad (\text{S28})$$

and rewrite $1/\|\mathbf{r} - \mathbf{r}'\|$ using the Laplace expansion of the Coulomb potential (Eq. (S5)). Then, after interchanging the order of the summation over l, m and the two integrals, all factors containing \mathbf{r} and \mathbf{r}' are grouped together, leading to the desired result. \square

C. Extension of Multipole Expansion to General Inverse Power-Law Potential

We now extend this analysis to exponents other than $p = 1$. Just as before, we wish to derive three versions of the multipole expansion, corresponding to the three equations (S2) for interior charges, (S3) for exterior charges and (S4) for the interaction energy between the two regions. The key ingredient will be the generalization of the Laplace expansion of the Coulomb potential, discussed in [section S1 B 1](#), to the general case. All variants of the multipole expansion will then follow in a straight-forward manner.

Note that different generalizations of the multipole expansion for general exponents have been proposed in the past, either based on the use of Cartesian coordinates or modified spherical harmonics. These methods, however, are less suitable for many ML applications in which we require a more systematic expansion in terms of the (usual) spherical harmonics due to symmetry reasons.

1. Key ingredient: Laplace Expansion of General Power-Law Potential

What made the Laplace expansion of the Coulomb potential so powerful was the fact that the expression $1/\|\mathbf{r} - \mathbf{r}'\|$ could be written in a way that provided a separation of the \mathbf{r} and \mathbf{r}' dependence. Thus, in order to generalize the mutipole expansion to arbitrary $1/r^p$ potentials, we need to derive an analogous expansion of $1/\|\mathbf{r} - \mathbf{r}'\|^p$. We begin by stating this generalized result and provide some intuition. As before, readers can feel free to skip the proof and continue to the next subsection, in which this lemma is used to prove the actual multipole expansion theorems.

Lemma S1.5. *Let $\mathbf{r}, \mathbf{r}' \in \mathbb{R}^3$ such that $r < r'$ and $p \in \mathbb{R}_+$. Then,*

$$\frac{1}{\|\mathbf{r} - \mathbf{r}'\|^p} = \sum_{nlm} \frac{4\pi}{2l+1} A_{n,l}^p \frac{r^{l+2n}}{r'^{p+l+2n}} Y_l^m(\mathbf{r}') Y_l^m(\mathbf{r}), \quad (\text{S29})$$

where \sum_{nlm} is a shorthand for $\sum_{n=0}^{\infty} \sum_{l=0}^{\infty} \sum_{m=-l}^l$ and $A_{n,l}^p$ are suitable coefficients.

Compared to the special case of $p = 1$ presented in Equation S5, we observe that the general version is more complex: it requires a sum over an additional index n , rather than just l, m . This is what makes all potentials with $p \neq 1$ qualitatively different from the Coulomb potential. As briefly mentioned before, $p = 1$ is special because applying the (three-dimensional) Laplace operator to $1/r$, we obtain $\Delta 1/r = 0$ for $r \neq 0$. It is, from a deeper point of view, this fact that eliminates all coefficients other than those where $n = 0$ in the Coulombic case.

Proof. The proof is similar to the one of Lemma (S5), except that there is one extra step that leads to the more complicated multipole expansion also requiring a sum over n . The first step again uses simple algebra to rewrite the denominator as

$$\frac{1}{\|\mathbf{r} - \mathbf{r}'\|^p} = \frac{1}{(r^2 + r'^2 - 2rr' \cos \gamma)^{\frac{p}{2}}} = \frac{1}{r'^p \left(\left(\frac{r}{r'}\right)^2 + 1 - 2\left(\frac{r}{r'}\right) \cos \gamma \right)^{\frac{p}{2}}}, \quad (\text{S30})$$

where $\cos \gamma = \hat{\mathbf{r}} \cdot \hat{\mathbf{r}'}$ is the angle between \mathbf{r} and \mathbf{r}' .

For the next step, we will use a set of special functions called Gegenbauer polynomials (also known as ultraspherical polynomials), which are a generalization of Legendre polynomials. These obey the relation

$$\frac{1}{(1 - 2cx + x^2)^{p/2}} = \sum_{q=0}^{\infty} C_q^{p/2}(c)x^q. \quad (\text{S31})$$

for any $x, c \in \mathbb{R}$ with $|c| < 1$ and $|x| < 1$ (alternatively, one could use this as a way to define the Gegenbauer polynomials in terms of a generating function). Note that for $p = 1$, the Gegenbauer polynomials $C_q^{1/2}$ reduce to the Legendre polynomials. We can use this identity with $x = r/r'$ and $c = \cos \gamma = \hat{\mathbf{r}} \cdot \hat{\mathbf{r}'}$, which leads us to

$$\frac{1}{\|\mathbf{r} - \mathbf{r}'\|^p} = \sum_{q=0}^{\infty} C_q^{p/2}(\hat{\mathbf{r}} \cdot \hat{\mathbf{r}'}) \frac{r'^q}{r^{p+q}}. \quad (\text{S32})$$

Note that we have called the index of summation q rather than l , for reasons that we will now explain.

In our application, we require a form of the multipole expansion that is written in terms of the spherical harmonic functions Y_l^m . Thus, we need to find a way to express $C_q^{p/2}$ in terms of spherical harmonics. While no direct such relation is known to the authors, we can exploit the fact that Gegenbauer polynomials share many similarities to the Legendre polynomials: for all $p > 0$, $C_q^{p/2}$ is a polynomial of degree q . If q is even (odd), then the function $C_q^{p/2}$ is even (odd) as well. Thus, using the analogous properties of the Legendre polynomials, we can see that there must exist some coefficients $\tilde{A}_{q,l}^p$ that allow us to express $C_q^{p/2}$ as a linear combination of Legendre polynomials P_l

$$C_q^{p/2} = \sum_l' \tilde{A}_{q,l}^p P_l, \quad (\text{S33})$$

where the prime in the summation indicates that l runs over $l = q, q-2, q-4, \dots$ up to 0 or 1 depending on whether q is even or odd due to the parity of both P_l and C_q . We thus obtain

$$\frac{1}{\|\mathbf{r} - \mathbf{r}'\|^p} = \sum_{q=0}^{\infty} \sum_l' \tilde{A}_{q,l}^p P_l(\hat{\mathbf{r}} \cdot \hat{\mathbf{r}'}) \frac{r'^q}{r^{p+q}}. \quad (\text{S34})$$

We can already observe a key difference to the electrostatic special case: For the Coulomb potential, the term decaying as $1/r^{1+l}$ only had an angular dependence of the form P_l , while for general p , the term decaying as $1/r^{p+q}$ requires multiple angular terms P_l with $l = q, q-2, \dots$ and so on. Equivalently, and more conveniently for our application, we can group together all terms that belong to the same value of l and say that the term with an angular dependence of P_l has radial dependence $1/r^{p+q}$ for $q = l, l+2, l+4, \dots$. This can be reparametrized as $q = l + 2n$ for $n = 0, 1, 2, \dots$. Thus, we obtain the general relation

$$\sum_{q=0}^{\infty} \sum_{l=q, q-2, \dots} f(q, l) = \sum_{l=0}^{\infty} \sum_{n=0}^{\infty} f(l+2n, l) \quad (\text{S35})$$

which can be applied to our case to yield

$$\frac{1}{\|\mathbf{r} - \mathbf{r}'\|^p} = \sum_{l=0}^{\infty} \sum_{n=0}^{\infty} \tilde{A}_{l+2n, l}^p P_l(\hat{\mathbf{r}} \cdot \hat{\mathbf{r}'}) \frac{r'^{l+n}}{r^{p+l+n}} =: \sum_{l=0}^{\infty} \sum_{n=0}^{\infty} A_{n, l}^p P_l(\hat{\mathbf{r}} \cdot \hat{\mathbf{r}'}) \frac{r'^{l+n}}{r^{p+l+n}}, \quad (\text{S36})$$

where for convenience, we have re-indexed the coefficients \tilde{A}_{l+2n}^p as $A_{n,l}^p$.

Finally, we can again use the spherical harmonics addition theorem

$$P_l(\hat{\mathbf{r}} \cdot \hat{\mathbf{r}}') = \sum_{m=-l}^l \frac{4\pi}{2l+1} Y_l^m(\hat{\mathbf{r}}') Y_l^m(\hat{\mathbf{r}}) \quad (\text{S37})$$

to obtain the final expression

$$\frac{1}{\|\mathbf{r} - \mathbf{r}'\|^p} = \sum_{nlm} \frac{4\pi}{2l+1} A_{n,l}^p \frac{r^{l+2n}}{r'^{p+l+2n}} Y_l^m(\mathbf{r}') Y_l^m(\mathbf{r}) \quad (\text{S38})$$

which concludes the proof. \square

2. Interior Charges

We can now discuss the three versions of the multipole expansion for general exponent p . As for the Coulombic case, the most challenging part of the derivation is the Laplace expansion in Equation (S29). If we accept this result, deriving the multipole expansion is just a simple extra step consisting of regrouping terms.

Theorem S1.6. *Let $\rho^<$ be a localized charge density which is entirely contained within a cutoff radius r_{cut} . The resulting “electrostatic” (inverse power-law) potential $V^<(\mathbf{r}')$ with exponent p evaluated at some point \mathbf{r}' outside of the cutoff is given by*

$$V^<(\mathbf{r}') = \sum_{nlm} M_{nlm}^< \frac{1}{r'^{p+l+2n}} Y_l^m(\hat{\mathbf{r}}'), \quad (\text{S39})$$

with coefficients

$$M_{nlm}^< = \frac{4\pi}{2l+1} A_{n,l}^p \int_0^{r_{\text{cut}}} d^3\mathbf{r} r^{l+2n} Y_l^m(\hat{\mathbf{r}}) \rho^<(\mathbf{r}), \quad (\text{S40})$$

and where \sum_{nlm} is a shorthand for $\sum_{n=0}^{\infty} \sum_{l=0}^{\infty} \sum_{m=-l}^l$.

Proof. From the superposition principle, the potential generated by the interior charges is given by

$$V^<(\mathbf{r}') = \int_0^{r_{\text{cut}}} d^3\mathbf{r} \frac{\rho^<(\mathbf{r})}{\|\mathbf{r} - \mathbf{r}'\|^p}. \quad (\text{S41})$$

Rewriting $1/\|\mathbf{r} - \mathbf{r}'\|^p$ using the generalized Laplace expansion (Equation (S29)), we obtain

$$V^<(\mathbf{r}') = \int_0^{r_{\text{cut}}} d^3\mathbf{r} \rho^<(\mathbf{r}) \sum_{nlm} \frac{4\pi}{2l+1} A_{n,l}^p \frac{r^{l+2n}}{r'^{p+l+2n}} Y_l^m(\mathbf{r}) Y_l^m(\mathbf{r}') \quad (\text{S42})$$

If $\rho^<$ is continuous, it is permissible to interchange the summation with the integral, which leads to

$$V^<(\mathbf{r}') = \sum_{nlm} \underbrace{\left[\frac{4\pi A_{n,l}^p}{2l+1} \int_0^{r_{\text{cut}}} d^3\mathbf{r} \rho^<(\mathbf{r}) r^{l+2n} Y_l^m(\mathbf{r}) \right]}_{=: M_{nlm}^<} \frac{1}{r'^{p+l+2n}} Y_l^m(\mathbf{r}') = \sum_{nlm} M_{nlm}^< \frac{1}{r'^{p+l+2n}} Y_l^m(\mathbf{r}') \quad (\text{S43})$$

with

$$M_{nlm}^< = \frac{4\pi A_{n,l}^p}{2l+1} \int_0^{r_{\text{cut}}} d^3\mathbf{r} \rho^<(\mathbf{r}) r^{l+2n} Y_l^m(\mathbf{r}). \quad (\text{S44})$$

Thus, using the identical steps as for the Coulombic case, we obtain the desired result. \square

3. Exterior Charges

Just as for the Coulomb potential, we can now flip the roles between the exterior and interior regions: the charges are now outside, and we wish to compute the potential generated by these in the interior region. The result is analogous to the previous case, except that all factors of r^{l+2n} and $1/r^{p+l+2n}$ switch roles.

Theorem S1.7. *Let $\rho^>$ be a charge density which is entirely contained outside of a cutoff radius r_{cut} . The resulting “electrostatic” (inverse power-law) potential $V^>(\mathbf{r})$ with exponent p evaluated at some point \mathbf{r} inside of the cutoff is given by*

$$V^>(\mathbf{r}) = \sum_{nlm} M_{nlm}^> r^{l+2n} Y_l^m(\hat{\mathbf{r}}), \quad (\text{S45})$$

with coefficients

$$M_{nlm}^> = \frac{4\pi}{2l+1} A_{n,l}^p \int_{r_{\text{cut}}}^{\infty} d^3\mathbf{r}' \frac{1}{r'^{p+l+2n}} Y_l^m(\hat{\mathbf{r}}') \rho^>(\mathbf{r}'), \quad (\text{S46})$$

and where \sum_{nlm} is a shorthand for $\sum_{n=0}^{\infty} \sum_{l=0}^{\infty} \sum_{m=-l}^l$.

Proof. The proof is completely analogous to the various versions presented so far, consisting of the steps:

1. Start from the expression $V^>(\mathbf{r}) = \int_{r_{\text{cut}}}^{\infty} d^3\mathbf{r}' \frac{\rho^>(\mathbf{r}')}{\|\mathbf{r}-\mathbf{r}'\|^p}$ (Equation (S3))
2. Use the Laplace expansion (Equation (S29)) for $1/\|\mathbf{r}-\mathbf{r}'\|^p$
3. Interchange the order of summation (over n, l, m) and integration
4. Regroup factors that depend on \mathbf{r}' to get the coefficients $M_{nlm}^>$

□

4. Inter-Regional Interaction Energy

Finally, we discuss how to compute the “inter-regional” interaction energy E_{int} between the charges in the two regions, namely

$$E_{\text{int}} = \int_0^{r_{\text{cut}}} d^3\mathbf{r} \int_{r_{\text{cut}}}^{\infty} d^3\mathbf{r}' \frac{\rho^<(\mathbf{r})\rho^>(\mathbf{r}')}{\|\mathbf{r}-\mathbf{r}'\|^p}. \quad (\text{S47})$$

As for the Coulomb potential, obtaining a multipolar expression for this interaction energy will be useful to obtain a physical interpretation of ML models that are built on top of the LODE features.

Theorem S1.8. *The interaction energy E_{int} between the interior charges $\rho^<$ and exterior charges $\rho^>$ for a general exponent $p \neq 1$ can be computed as*

$$E_{\text{int}} = \sum_{nlm} \frac{2l+1}{4\pi A_{n,l}^p} M_{nlm}^> M_{nlm}^<. \quad (\text{S48})$$

where $M_{nlm}^>$ and $M_{nlm}^<$ are the exterior and interior multipole moments defined in the two previous subsections [S1 C 3](#) and [S1 C 2](#), respectively.

Proof. The proof is completely analogous to the various versions presented so far, consisting of the steps:

1. Start from the expression $E_{\text{int}} = \int_0^{r_{\text{cut}}} d^3\mathbf{r} \int_{r_{\text{cut}}}^{\infty} d^3\mathbf{r}' \frac{\rho^<(\mathbf{r})\rho^>(\mathbf{r}')}{\|\mathbf{r}-\mathbf{r}'\|^p}$ (Equation (S4))
2. Use the Laplace expansion (Equation (S29)) for $1/\|\mathbf{r}-\mathbf{r}'\|^p$
3. Interchange the order of summation (over n, l, m) and integration
4. Group all factors that depend on \mathbf{r}' together to get the coefficients $M_{nlm}^>$, and those that depend on \mathbf{r} together to get the coefficients $M_{nlm}^<$

□

D. Remark On Conventions and Prefactors

The definitions of the various multipolar quantities in this work might differ from those found in some of the literature. We briefly summarize some conventions.

- We write all results using the real versions of the spherical harmonics, since these are more suitable for our applications in which all functions are real-valued. The actual software implementation also uses real spherical harmonics due to more efficient storage.

All results do however also apply if we use complex spherical harmonics instead, since the transformation between the two is unitary, with a single modification. In most places, the spherical harmonics appear in pairs. One of the two spherical harmonics (which one does not matter) will then need to get replaced by the complex conjugate. For the Laplace expansion of the Coulomb potential, this is explicitly shown at the end of the proof of Lemma S5.

- We refer to the coefficients $M_{lm}^<$ (or $M_{nlm}^<$) that characterize **interior** charges as **interior** multipole moments. On the other hand, some works would call this the **exterior** multipole expansion, since we evaluate the potential at a point \mathbf{r}' in the exterior region (and vice versa if the charges are outside). We decided to use this terminology because the focus in this work is on the atoms (charges), rather than where the potential is evaluated.
- Our definition of multipole moments, e.g. those in sections S1 B 2 and S1 B 3 contain the prefactors of $\frac{4\pi}{2l+1}$. It would, however, also be possible not to include this factor in the coefficient itself, and to keep it in the final summation. This clearly does not affect any of the conclusions. The current convention was chosen to maximize the mathematical analogies to the density based descriptors which are discussed in more detail in the next section within this Supporting Information.

S2. PHYSICAL INTERPRETATION AND OPTIMIZATION OF LODE REPRESENTATION

A. Overview of this section

In this section, we provide a complete and mostly self contained description of the mathematical theory behind the LODE descriptors that are used throughout the main text. We begin by reviewing a general mathematical framework for the construction of atomic descriptors that unifies LODE and many SR features (e.g. SOAP) that is described in.² We believe that the way we present the concepts here will help to better see the connection between the different representations as well as the multipole expansion discussed in the previous section in this Supporting Information.

B. General Framework for Atomic Representations

We begin by providing a quick summary of a general framework to construct atomic representations, using the better-established SR descriptors as an example. We are given an atomic structure consisting of N atoms (with or without periodic boundary conditions) indexed as $i = 1, 2, \dots, N$, whose position vectors are denoted by \mathbf{r}_i and chemical species by $a_i \in \{\text{H, He, Li, } \dots\}$.

We start by defining a density contribution function g , a popular choice being a Gaussian function

$$g(\mathbf{r}) \propto \exp(-\mathbf{r}^2/2\sigma^2), \tag{S49}$$

where σ is a parameter controlling the width, as shown in section S2 Ba. Different normalizations for the Gaussian are possible, but the specific choice is irrelevant to this discussion.

This density contribution function g is then used to define a density function ρ over the entire structure, $\rho(\mathbf{r}) = \sum_j g(\mathbf{r} - \mathbf{r}_j)$ shown in section S2 Bb. This function ρ is not directly related to any physical quantity (e.g. the electron density), but contains the information about the location of all atoms in the structure. For instance, we could imagine that we “hide” all atoms from section S2 Bb, and only show the density function. Since the locations of the atoms correspond to peaks in ρ , we can reconstruct the atomic positions (up to some precision that is determined by the smearing σ).

To describe the local neighborhood around an atom i rather than the entire structure, we use the atom centered density $\rho_i(\mathbf{r}) = \rho(\mathbf{r} + \mathbf{r}_i)$, truncated at some cutoff radius $r = \|\mathbf{r}\| \leq r_{\text{cut}}$, i.e. only the portion of ρ around \mathbf{r}_i (the cutoff is shown with dashed lines in section S2 Bc).

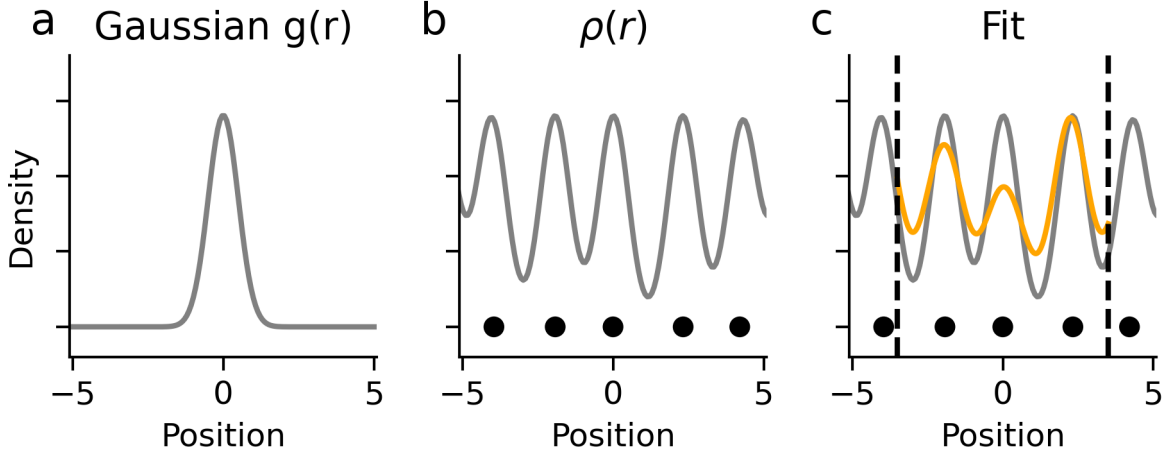


Figure S4. Visualization of the steps involved to generate short-range descriptors, including the popular SOAP descriptor. a: Density contribution function showing the density for a single atom. b: Density of the structure as a whole, obtained by considering superpositions of the function in part a for each atom. c: Fitting the target density within some cutoff requires the specification of some fitting parameters, which contain the information on the atomic positions.

For computational applications, it is necessary to describe the neighborhood of atom i using a discrete set of coefficients, rather than an abstract function ρ_i . Thus, we choose a set of orthonormal basis functions B_{nlm} , which for symmetry reasons are typically of the form $B_{nlm}(\mathbf{r}) = R_{nl}(r)Y_l^m(\hat{\mathbf{r}})$, where $R_{nl}(r)$ are the radial basis functions and $Y_l^m(\hat{\mathbf{r}})$ are the real spherical harmonics describing the angular part. Any continuous function including ρ_i can then be written as the linear combination of the basis functions

$$\rho_i(\mathbf{r}) = \sum_{nlm} \rho_{i,nlm} B_{nlm}(\mathbf{r}) = \sum_{nlm} \rho_{i,nlm} R_{nl}(r) Y_l^m(\hat{\mathbf{r}}), \quad (\text{S50})$$

with coefficients $\rho_{i,nlm}$ given by the inner product of the basis function with the target density ρ_i ,

$$\rho_{i,nlm} = \int_0^{r_{\text{cut}}} d^3\mathbf{r} R_{nl}(r) Y_l^m(\hat{\mathbf{r}}) \rho_i(\mathbf{r}). \quad (\text{S51})$$

The coefficients $\rho_{i,nlm}$ contain the information about the atomic positions around atom i , and can thus be used in ML applications to predict atomic properties. In reality, in most applications, the coefficients are not used directly: for instance, if the target property is invariant under rotations (e.g. the energy), rotationally invariant combinations of these coefficients are used. This can also be generalized to arbitrary transformation behaviors with respect to rotations.

The SR nature of the descriptor arises from the use of a quickly decaying function for the density contribution function g , common choices being the aforementioned Gaussian function^{3,4} and the infinitely sharp limit of delta distributions $g(\mathbf{r}) \rightarrow \delta(\mathbf{r})$,^{5,6} which in turn enables efficient predictions of materials properties scaling linearly with the number of atoms. More details on SR descriptors are discussed in the review article.²

C. LODE for Coulombic Interactions

While this framework was originally developed for SR descriptors, it permits an elegant extension to arbitrary LR interactions. By changing the density contributions g to a slowly decaying function, we obtain a new density function $\rho(\mathbf{r})$ for which even the local neighborhood around an atom i contains more information about far-away atoms.

Motivated by the fact that the most important LR interaction is the electrostatic one, the original work on LODE⁷ used a density contribution of the form

$$g_{\text{Coulomb}}(\mathbf{r}) = \frac{\text{erf}(r/\sqrt{2}\sigma)}{r}, \quad (\text{S52})$$

where $\text{erf}(x)$ is the error function. This corresponds to the Coulomb potential of a Gaussian charge density, commonly used for Ewald summation.¹ As for the Coulomb potential, this function asymptotically behaves as $1/r$ for $r \rightarrow \infty$,

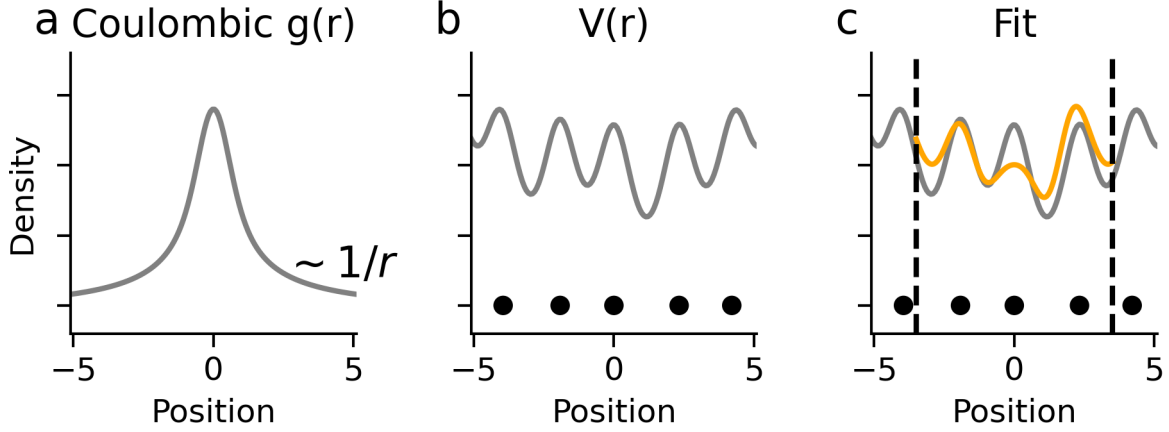


Figure S5. Visualization of the steps involved to generate the LODE descriptors. a: Density contribution function showing the density for a single atom. As opposed to a Gaussian, the functions now decay as $1/r$. b: Density of the structure as a whole, obtained by considering superpositions of the function in part a for each atom. c: Fitting the target density within some cutoff requires the specification of some fitting parameters, which contain the information on the atomic positions, now also including atoms outside of the cutoff due to the slow decay.

while the singularity at $r = 0$ of the bare Coulomb potential has been smeared out (section S2 Ca). To differentiate this Coulombic density from the SR ones, as well as to emphasize the mathematical analogy to the Coulomb potential of the structure, we write $V(\mathbf{r}) = \sum_j g_{\text{Coulomb}}(\mathbf{r} - \mathbf{r}_j)$ rather than $\rho(\mathbf{r})$ for the total density which is shown in section S2 Cb.

Just as for SR densities, for each center atom i , an atomic descriptor is constructed by first defining the shifted (atom centered) version of the density, $V_i(\mathbf{r}) = V(\mathbf{r} - \mathbf{r}_i)$ defined up to $r = \|\mathbf{r}\| \leq r_{\text{cut}}$. To get a discrete set of coefficients, this density is projected onto the basis functions B_{nlm} , leading to coefficients

$$V_{i,nlm} = \int_0^{r_{\text{cut}}} d^3\mathbf{r} R_{nl}(r) Y_l^m(\hat{\mathbf{r}}) V_i(\mathbf{r}). \quad (\text{S53})$$

The key idea is that due to the slow decay, even atoms outside the cutoff will provide significant contributions to the interior density (section S2 Cc). The only conceptual difference to the SR version is thus a different choice of the density contribution $g(\mathbf{r})$, which allows us to easily reuse all ML methods that work for SR models and combine them with the LR modifications. This is the key idea of the LODE framework.

Note that for systems with periodic boundary conditions, the sum $V(\mathbf{r}) = \sum_j g(\mathbf{r} - \mathbf{r}_j)$ is understood to include all periodic images. While only the nearest ones are sufficient for SR models due to the (at least exponentially) fast decay of $g(r)$, the LR descriptors require a more proper treatment of the infinitely many periodic images using an Ewald-like Fourier space formulation, which is discussed in section S2 H. Thus, while conceptually close to SR densities, actual implementations to compute the coefficients $V_{i,nlm}$ will be quite different from their SR counterparts.

D. Extension to Arbitrary Long-Range Descriptors

Given the diversity of $1/r^p$ interactions, $1/r^6$ being the most important from a physical point of view, it is natural to extend LODE to other exponents p . This can be achieved by finding a function $g(\mathbf{r})$ behaving as $1/r^p$ for $r \rightarrow \infty$, while being monotonous in r and differentiable in the entire space. We use

$$g_p(\mathbf{r}) = \frac{1}{\Gamma\left(\frac{p}{2}\right)} \frac{\gamma\left(\frac{p}{2}, \frac{r^2}{2\sigma^2}\right)}{r^p}, \quad (\text{S54})$$

where $\Gamma(x)$ is the Gamma function, and $\gamma(a, x)$ is the lower incomplete Gamma function. Up to different scaling, this is a functional form that was first introduced in⁸ and extended in.^{9,10}

It should be noted that (S54) is not simply the effective $1/r^p$ potential generated by a Gaussian charge density, which would naively be the first candidate function. In fact, such an approach would not work for exponents $p \geq 3$ due to the strong singularity at the origin. Nevertheless, (S54) reduces to Equation (S52) for $p = 1$. Some mathematical

details of this density contribution function, including the fact that it satisfies all desired properties, are discussed in [section S3](#).

Summarizing the general recipe to generate the descriptors discussed so far, the methods are defined by the choices of (1) the density contributions $g(\mathbf{r})$ and (2) the radial basis functions $R_{nl}(r)$ on which the resulting density is projected. Different SR models as well as the transition to various LR models is primarily characterized by the choice of $g(\mathbf{r})$. In the next two subsections, we show how a suitable choice of R_{nl} leads to a clean physical interpretation of descriptors as well as more efficient implementations. While all $1/r^p$ potentials share many properties with the Coulombic special case of $p = 1$, the general case is more complicated and is discussed separately after building a good intuition based on the Coulomb potential first.

E. Physical Interpretation and Optimizations for the Coulombic Case

So far, we have provided a mathematical recipe to compute both SR and LODE features, including the generalization to arbitrary exponents p . We will now show how a more detailed mathematical analysis can provide both a more physical interpretation of these coefficients, as well as a mathematical optimization method for more efficient implementations.

In terms of mathematical prerequisites, the rest of this section will make use of two key properties of spherical harmonics. The first one is the mutual orthogonality, explicitly given by

$$\int_{S^2} dS Y_l^m(\hat{\mathbf{r}}) Y_{l'}^{m'}(\hat{\mathbf{r}}) = \int_0^{2\pi} d\phi \int_0^\pi d\theta \sin\theta Y_l^m(\theta, \phi) Y_{l'}^{m'}(\theta, \phi) = \delta_{l,l'} \delta_{m,m'}, \quad (\text{S55})$$

where S^2 is the unit sphere characterized by the two spherical angles θ and ϕ . The second property is that any continuous (more generally, L^2) function f in the angles (θ, ϕ) (on the sphere S^2) can be expressed as a Fourier series

$$f = \sum_{l,m} f_{l,m} Y_l^m, \quad (\text{S56})$$

with coefficients

$$f_{l,m} = \int_{S^2} dS Y_l^m f. \quad (\text{S57})$$

Summarizing the two properties more compactly, we can say that the spherical harmonics form an orthonormal (Schauder) basis for the (L^2)-space of functions on the unit sphere.

The last key ingredient for our analysis is the multipole expansion from electrostatics, which was already used in.¹¹ That work in fact claimed that

... neither the atom density ρ_i nor the associated potential V_i correspond to physical quantities ...

and that only certain combinations of $\rho_{i,nlm}$ and $V_{i,nlm}$

... entail(s) formal similarities with physics-based electrostatic models.

We will show that a more careful analysis using the multipole expansion does in fact provide a direct physical interpretation to both sets of coefficients $\rho_{i,nlm}$ and $V_{i,nlm}$ in terms of electrostatic quantities. This connection also provides us with an explicit recipe for faster algorithmic implementations. A self contained review of the multipole expansion for the Coulomb potential, as well as an extension to arbitrary exponents p that was performed as part of this work, are discussed in [section S1 C](#). For readers only interested to the applications to atomistic descriptors, we briefly summarize the main results.

Let ρ_i be the atomic density around atom i , but now without the restriction due to a cutoff radius. As shown in [Figure S1a](#), we split it up into an interior part $\rho_i^<$ and exterior part $\rho_i^>$, each only containing the density inside / outside the cutoff radius r_{cut} , respectively, such that $\rho_i = \rho_i^< + \rho_i^>$. For the rest of this document, we shall denote by \mathbf{r} (\mathbf{r}') a point inside (outside) the cutoff, i.e. $r = \|\mathbf{r}\| < r_{\text{cut}}$ ($r' = \|\mathbf{r}'\| > r_{\text{cut}}$).

The classical version of the multipole expansion is discussed in many textbooks on electrodynamics,¹ and is illustrated in [Figure S1b](#): The electric potential $V_i^<(\mathbf{r}')$ generated by a localized (interior) charge density $\rho_i^<$ evaluated at some point \mathbf{r}' in the exterior region can be written as

$$V_i^<(\mathbf{r}') = \sum_{lm} M_{i,lm}^< \frac{1}{r'^{l+1}} Y_l^m(\hat{\mathbf{r}}'), \quad (\text{S58})$$

with coefficients

$$M_{i,lm}^< = \int_0^{r_{\text{cut}}} d^3\mathbf{r} r^l Y_l^m(\hat{\mathbf{r}}) \rho_i^<(\mathbf{r}), \quad (\text{S59})$$

which are called (interior) multipole moments and completely characterize the potential in the exterior region. Intuitively, this corresponds to a Fourier-like expansion of the interior density into terms of higher and higher frequencies.

Comparing this with (S51), we can see that the SR features $\rho_{i,nlm}$ can be made to exactly match the interior multipole moment $M_{i,lm}^<$ of the density $\rho_i^<$ within the cutoff radius around atom i , if we choose the radial basis function $R_{nl}(r) = r^l$, which provides us with SR features that have an exact electrostatic interpretation.

Flipping the roles around, it is possible to compute the electrostatic potential $V_i^>(\mathbf{r})$ generated by the exterior charges $\rho_i^>$, evaluated at an interior point \mathbf{r} , as is shown in Figure S1c. Similar to the previous case, the potential is completely characterized by coefficients $M_{i,lm}^>$, the exterior multipole moments, such that

$$V_i^>(\mathbf{r}) = \sum_{lm} M_{i,lm}^> r^l Y_l^m(\hat{\mathbf{r}}), \quad (\text{S60})$$

$$M_{i,lm}^> = \int_{r_{\text{cut}}}^{\infty} d^3\mathbf{r}' \frac{1}{r'^{l+1}} Y_l^m(\hat{\mathbf{r}}') \rho_i^>(\mathbf{r}'). \quad (\text{S61})$$

As for the interior version, this can be interpreted as a decomposition of the exterior charge density $\rho^>$ into (angular) frequency components.

To show the analogy to the LODE coefficients, we now project this density $V_i^>(\mathbf{r})$ onto basis functions $B_{nlm}(\mathbf{r}) = R_{nl}(r)Y_l^m(\hat{\mathbf{r}})$. From the orthonormality of the spherical harmonics, we get

$$V_{i,nlm}^> = \int_0^{r_{\text{cut}}} d^3\mathbf{r} R_{nl}(r) Y_l^m(\hat{\mathbf{r}}) V_i^>(\mathbf{r}) = M_{i,lm}^> \int_0^{r_{\text{cut}}} dr r^{2+l} R_{nl}(r) \quad (\text{S62})$$

Thus, we can see that the projection of $V_i^>$ allows us to recover the exterior multipole moment $M_{i,lm}^>$ up to a prefactor that only depends on the choice of radial basis. Choosing the same radial function $R_{nl}(r) = R_l(r) = r^l$, we obtain

$$V_{i,lm} = C_l M_{i,lm}^>, \quad C_l = \frac{r_{\text{cut}}^{3+2l}}{3+2l}. \quad (\text{S63})$$

Thus, if it was possible to extract from the full potential $V_i(\mathbf{r})$ the part $V_i^>(\mathbf{r})$ that corresponds to the contribution of exterior charges, a comparison with Equation (S53) shows that the LODE coefficients $V_{i,nlm}$ correspond precisely to the exterior multipole moment $M_{i,lm}^>$, for the charge density $\rho_i^>$ defined relative to the central atom i . Eliminating the interior part $\rho_i^<$ is simple in principle, since this can be implemented using the same methods as for SR densities.

There are two important messages that we can learn from this analysis. Firstly, beyond the formal analogy originally proposed in¹¹ for the special case of linear models, we can see that the coefficients $\rho_{i,nlm}$ and a suitable modification of $V_{i,nlm}$ correspond exactly to the interior and exterior multipole moments of the “density” $\rho_i(\mathbf{r})$ centered around atom i , if we interpret it as a charge density (see remarks in section S2H of the Supporting Information regarding the sign conventions and the more subtle treatment of different chemical species) separated into two regions by the cutoff radius r_{cut} around center atom i .

Secondly, we can connect this to a significant speedup of codes implementing LODE. While typical approaches for ML models use a large number of radial basis functions, $n = 1, 2, \dots, n_{\text{max}}$ on the order of $4 \sim 10$, this analysis shows us that the entire LR information about atoms outside of the cutoff can be captured by using a single radial basis function, namely r^l . This results in a reduction of the computational cost as well as memory of LODE by a factor of n_{max} , which can be close to an order of magnitude.

F. Physical Interpretation and Optimizations for General Exponents

We now extend this analysis to exponents other than $p = 1$. Firstly, we need to start by deriving a generalization of the multipole expansion that is suitable for our use case. While different such forms have been proposed, either based on the use of Cartesian coordinates or modified spherical harmonics, these methods are less suitable for many ML applications, that require a more systematic expansion in terms of the (usual) spherical harmonics.

Stating the main result first, we will show that the potential $V_i^>(\mathbf{r})$ at a point \mathbf{r} in the interior region generated by an exterior charge density $\rho_i^>(\mathbf{r}')$ can be written as

$$V_i(\mathbf{r}) = \int_{r_{\text{cut}}}^{\infty} d^3\mathbf{r}' \frac{\rho_i(\mathbf{r}')}{\|\mathbf{r} - \mathbf{r}'\|^p} = \sum_{nlm} M_{i,nlm}^> r^{l+2n} Y_l^m(\hat{\mathbf{r}}), \quad (\text{S64})$$

where $M_{i,nlm}^>$ are suitable generalizations of the multipole moments that completely characterize the potential within the cutoff sphere. Similarly to the Coulombic special case, we can extract these coefficients and use them as inputs to a ML model using a suitable radial basis.

This form shows one key difference: The sum now also runs over $n = 0, 1, 2$, etc., indicating a more complicated radial dependence. The underlying mathematical reason is the fact that the Coulomb potential $g(\mathbf{r}) = 1/r$ is a solution to the Laplace equation $\Delta g = 0$ for $\mathbf{r} \neq 0$, while this is no longer true for any other $p \neq 1$.

Just as for the Coulombic case, we can extract the coefficients $M_{i,nlm}^>$ by choosing an appropriate set of radial basis functions $R_{nl}(r)$, the extra complication being the fact that for each angular channel l , the radial dependence is no longer a simple function with a single coefficient.

Nevertheless, keeping in mind that the term with $M_{i,nlm}^>$ in the generalized multipole expansion discussed in [section S1 C 3](#) contains information about the density decaying as $1/r^{p+l+2n}$, we propose the following method to pick the best exponents. First, one chooses a maximal decay exponent $1/r^{p_{\max}}$, with $p_{\max} = p + l_{\max}$. Then, we use all coefficients $M_{i,nlm}^>$ for which $p + l + 2n < p_{\max}$ as input to our ML model. This allows us to interpret the cutoff as a truncation in decay speed of the potentials. For a given level of desired accuracy p_{\max} , this approach requires about half as many coefficients compared to a more naive implementation in which a range of values for l and n are specified independently.

G. Building ML Models

A connection between LODE and the multipole expansion was already mentioned in previous work¹¹ for the special case of linear models, the key difference being that (1) beyond being a mathematical analogy, we see that the LODE coefficients are *precisely* suitably defined multipole moments characterizing the interior and exterior atoms, and (2) the mathematical equivalence arises directly at the level of the coefficients, and is not restricted to the use of linear models.

While our discussion so far has focused entirely on the descriptors, and not on the model, it is important to discuss the final step that will lead to the actual target property.

Just as for SR descriptors, we know that the power spectrum coefficients of the form

$$I[\rho \otimes V]_{nn'l} = \sum_{m=-l}^l \rho_{i,nlm} V_{i,n'lm} \quad (\text{S65})$$

for any n, n', l are rotationally invariant, and can thus be used as inputs to predict invariant target properties like the energy or charge of a system. While many other invariants can be constructed in a similar manner, these specific ones allow for a particularly simple interpretation.

To find an analogous quantity in electrostatics, let ρ once again be an arbitrary charge density, divided up into an interior and exterior part relative to some origin. The electrostatic interaction energy E_{int} between the interior charges $\rho^<$ and exterior charges $\rho^>$ (but not the interactions among themselves) is then given by

$$E_{\text{int}} = \int_0^{r_{\text{cut}}} d^3\mathbf{r} \int_{r_{\text{cut}}}^{\infty} d^3\mathbf{r}' \frac{\rho^<(\mathbf{r})\rho^>(\mathbf{r}')}{\|\mathbf{r} - \mathbf{r}'\|}. \quad (\text{S66})$$

Using the multipole expansion, it can be shown that

$$E_{\text{int}} = \sum_{lm} \frac{2l+1}{4\pi} M_{lm}^> M_{lm}^<. \quad (\text{S67})$$

In other words, the interaction energy is completely specified by knowing both the interior and exterior multipole moments of the charge distribution.

Beyond the Coulomb potential, the proof of the general multipole expansion for arbitrary exponents p can be used to also obtain the analogous result

$$E_{\text{int}} = \int_0^{r_{\text{cut}}} d^3\mathbf{r} \int_{r_{\text{cut}}}^{\infty} d^3\mathbf{r}' \frac{\rho^<(\mathbf{r})\rho^>(\mathbf{r}')}{\|\mathbf{r} - \mathbf{r}'\|^p} = \sum_{nlm} \frac{2l+1}{4\pi A_{l,n}^p} M_{nlm}^< M_{nlm}^>. \quad (\text{S68})$$

This can be compared with a linear model on the invariants in Eq. (S65) to predict the ‘‘atomic energy’’ E_i ,

$$E_i = \sum_{nn'lm} E_{nn'l} \rho_{i,nlm} V_{i,n'lm}. \quad (\text{S69})$$

Remembering that $\rho_{i,nlm}$ can be chosen to essentially correspond to $M_{nlm}^<$, while $V_{i,nlm}$ is $M_{nlm}^>$ for the charge density centered around atom i , we can see that we essentially recover the same mathematical form as the actual interaction energy between the two regions discussed in [section S1](#), with the extra flexibility of choosing the coefficients $E_{nn'l}$ in a non-uniform way. This is essentially the result presented in¹¹ rewritten in our notation, but with a cleaner separation of the connection between the multipole moments and the final model.

Clearly, the usage of the LODE coefficients $V_{i,nlm}$ is not restricted to linear models, and thanks to the mathematical closeness to SR approaches, any software architecture that works with SR descriptors should be capable of seamlessly integrating LODE to incorporate far-field contributions. Furthermore, the coefficients $V_{i,nlm}$ also possess the full equivariance discussed in,¹² and can thus be used to learn target properties of arbitrary tensorial character including dipole moments or electron densities.

H. Similarities and Differences of the LODE Density with the actual Coulomb Potential

The density function $V(\mathbf{r})$ that is used throughout the LODE framework is, by construction, closely related to the Coulomb potential. This is also why, to help the intuition, we informally refer to it as “the potential (field)” throughout this document. There are, however, two subtle differences to the actual Coulomb potential that one might compute, e.g. for MD simulations.

Summarized in a few sentences each, these are:

- Traditional methods for electrostatics including the Ewald based ones or PPPM split the potential into a SR and LR part, and treats the LR part with Fourier transforms for efficient evaluation. In this picture, LODE basically only is using the LR part.
- In MD, each atom is assigned a charge q_i (often one charge per chemical species), and the potential is the sum of the bare $1/r$ potential weighted by the charges. In LODE, each chemical species is assigned a separate density field, and are thus treated completely independently.

In the following two subsections, each of these points is discussed further.

1. Absence of SR-LR splitting

For the Coulombic case, it is possible to interpret the resulting function $g_{\text{Coulomb}}(r)$ as the effective potential generated by a Gaussian charge density, which is also how Ewald summation is often motivated in textbooks. This way of introducing the function $g(r)$ certainly has the advantage of being visually and physically pleasing, since the resulting method has a clear interpretation. In such a case, the total Coulomb potential is split into a SR and LR part, namely

$$\frac{1}{r} = g(r) + h(r) = \frac{\text{erf}(r/\sqrt{2}\sigma)}{r} + \frac{\text{erfc}(r/\sqrt{2}\sigma)}{r}, \quad (\text{S70})$$

where the second term $h(r)$ is the SR part containing the complementary error function $\text{erfc}(x) = 1 - \text{erf}(x)$.

Splitting the Coulomb potential in this way has the advantage that the first term is purely LR, and thus easy to calculate in practice using Fourier transforms, while the second term is SR, and can thus be efficiently evaluated in real space. In traditional molecular dynamics simulations, explicitly including the SR part is important to get accurate energy and force predictions. LODE, on the other hand, only includes the LR part of this decomposition, the idea being that the SR part is typically already well covered by established approaches.

2. Treatment of different chemical species

A second way in which the LODE density function $V(\mathbf{r})$ differs from the usual electrostatic potential is the treatment of different atomic species. At the simplest level, in traditional MD simulations, each atomic species is assigned a charge q (e.g. for NaCl, one could set $q_{\text{Na}} = +1$ and $q_{\text{Cl}} = -1$ in appropriate units). The “physical” electrostatic potential $V_{\text{Coulomb}}(\mathbf{r})$ then formally corresponds to the expression

$$V_{\text{Coulomb}}(\mathbf{r}) = \sum_j q_j g_{\text{bare}}(\|\mathbf{r} - \mathbf{r}_j\|), \quad (\text{S71})$$

where the sum runs over all atoms in the structure (in general, including periodic images), and $g_{\text{bare}}(r) = 1/r$ is the (bare) Coulomb potential. In other words, regardless of the number of chemical species present in the system, we only obtain one potential function $V_{\text{Coulomb}}(\mathbf{r})$.

For LODE, on the other hand, each species is treated separately. Taking NaCl as an example, we would then obtain two separate density functions, namely

$$V_{\text{Na}}(\mathbf{r}) = \sum_{j \in \text{Na}} g(\|\mathbf{r} - \mathbf{r}_j\|) \quad (\text{S72})$$

$$V_{\text{Cl}}(\mathbf{r}) = \sum_{j \in \text{Cl}} g(\|\mathbf{r} - \mathbf{r}_j\|), \quad (\text{S73})$$

where the sum in the first (second) line only runs over all Na (Cl) atoms, respectively, including their periodic images. Note also that the charges q_j in the summation has been removed. Furthermore, the bare potential $g_{\text{bare}}(r) = 1/r$ has been replaced by the appropriate smeared version $g(r)$. We shall not touch upon this point since it was already discussed in the previous subsection. These two functions could be called the ‘‘Na-potential’’ and ‘‘Cl-potential’’, respectively. The ‘‘physical’’ Coulomb potential, if we ignore the distinction between g_{bare} and g , then is simply the linear combination

$$V_{\text{Coulomb}}(\mathbf{r}) = q_{\text{Na}}V_{\text{Na}}(\mathbf{r}) + q_{\text{Cl}}V_{\text{Cl}}(\mathbf{r}). \quad (\text{S74})$$

From the point of view of ML models, it means that the information about the ‘‘physical’’ Coulomb potential is contained in the LODE potentials, but the latter still have more flexibility, and describe the location of the atoms separately for each species.

Clearly, in a data set containing atoms of N_a different species, there would be one such potential V_a for each species, where a runs over all possible such elements.

All the steps discussed in the main text are then separately applied to each of these potentials. Thus, after picking a center atom i for which we wish to compute the atom-centered features, we compute the potential function for species a centered around atom i , as $V_{ia}(\mathbf{r}) = V_a(\mathbf{r} - \mathbf{r}_i)$ and project onto a basis, leading to a set of coefficients $V_{ia,nlm}$ defined by

$$V_{ia} = \sum_{nlm} V_{ia,nlm} B_{nlm}. \quad (\text{S75})$$

One further subtlety has to be considered for periodic systems: for the traditional Ewald summation based methods, it can be shown that (for exponents $p < 3$, which includes the important Coulomb case) the well-definedness of the potential function requires that the unit cell as a whole is charge neutral. This condition is relatively easy to satisfy for systems, in which the charges q_j are chosen manually. On the other hand, as is apparent from equations (S72) and (S73), all terms in the summation are assigned the same charge. Physically, this problem can be solved by adding a homogeneous background charge of opposite sign to the system, as is also done for, e.g. the Jellium model.

S3. BEHAVIOR OF GENERAL DENSITY CONTRIBUTION FUNCTION

We show that the density contribution function

$$g(\mathbf{r}) = g(r) = \frac{1}{\Gamma\left(\frac{p}{2}\right)} \frac{\gamma\left(\frac{p}{2}, \frac{r^2}{2\sigma^2}\right)}{r^p}, \quad (\text{S76})$$

has the desired mathematical properties, namely that it behaves as $1/r^p$ as $r \rightarrow \infty$ while removing the singularity at the origin.

The Gamma function is defined as

$$\Gamma(a) = \int_0^\infty t^{a-1} e^{-t} dt, \quad (\text{S77})$$

while the lower incomplete Gamma function is defined similarly, but the integration range restricted to $[0, x]$:

$$\gamma(a, x) = \int_0^x t^{a-1} e^{-t} dt. \quad (\text{S78})$$

A. Long-Range Limit

In the limit as $r \rightarrow \infty$, we want $g(r)$ to asymptotically behave as $1/r^p$. From the definition of the lower incomplete Gamma function, we can immediately obtain

$$\gamma(a, x) = \int_0^x t^{a-1} e^{-t} dt \xrightarrow{x \rightarrow \infty} \int_0^\infty t^{a-1} e^{-t} dt = \Gamma(a) \quad (\text{S79})$$

Thus, we can indeed see that

$$g(r) \sim \frac{1}{r^p} \quad \text{as } r \rightarrow \infty, \quad (\text{S80})$$

where the equivalence relation $f(x) \sim g(x)$ for $x \rightarrow x_0$ means that f and g asymptotically behave in the same way, formally defined as $\lim_{x \rightarrow x_0} \frac{f(x)}{g(x)} = 1$.

B. Short-Range Limit

To convince ourselves that the singularity at $r = 0$ is properly taken care of, we can use the asymptotic expansion

$$\gamma(a, x) = \frac{x^a}{a} + O(x^{a+1}) \quad (\text{S81})$$

as $x \rightarrow 0$, which can directly be obtained from Taylor expanding the exponential function, and using Fubini's theorem to interchange the order of summation and integration (since the integrand is absolutely integrable):

$$\gamma(a, x) = \int_0^x t^{a-1} \sum_{n=0}^{\infty} \frac{(-1)^n t^n}{n!} dt = \sum_{n=0}^{\infty} \frac{(-1)^n}{n!} \int_0^x t^{a-1} t^n dt = \sum_{n=0}^{\infty} \frac{(-1)^n}{n!} \frac{x^{a+n}}{a+n} \quad (\text{S82})$$

$$= \frac{1}{a} x^a + O(x^{a+1}). \quad (\text{S83})$$

Using this, we can see that the limit at $r \rightarrow 0$ is indeed a well defined nonzero value, namely

$$\lim_{r \rightarrow 0} g(r) = \lim_{r \rightarrow 0} \frac{1}{\Gamma\left(\frac{p}{2}\right)} \frac{\gamma\left(\frac{p}{2}, \frac{r^2}{2\sigma^2}\right)}{r^p} = \lim_{r \rightarrow 0} \frac{1}{\Gamma\left(\frac{p}{2}\right)} \cdot \frac{1}{\frac{p}{2}} \left(\frac{r^2}{2\sigma^2}\right)^{\frac{p}{2}} \cdot \frac{1}{r^p} = \frac{1}{\Gamma\left(\frac{p+2}{2}\right) (2\sigma^2)^{\frac{p}{2}}}. \quad (\text{S84})$$

with corrections that are quadratic in r for small nonzero $r > 0$.

C. Coulombic Special Case

We begin by showing that for the special case of $p = 1$, we recover the Coulomb potential of a Gaussian density

$$g_{\text{Coulomb}}(r) = \frac{\text{erf}(r/\sqrt{2}\sigma)}{r}. \quad (\text{S85})$$

Comparing with the general expression, it suffices to show that

$$\text{erf}(r/\sqrt{2}\sigma) = \frac{\gamma\left(\frac{1}{2}, \frac{r^2}{2\sigma^2}\right)}{\Gamma(1/2)} = \frac{\gamma\left(\frac{1}{2}, \frac{r^2}{2\sigma^2}\right)}{\sqrt{\pi}} \quad (\text{S86})$$

since the factor of $1/r$ is common to both. This equality follows directly from the definition of the error function

$$\text{erf}z = \frac{2}{\sqrt{\pi}} \int_0^z e^{-t^2} dt \stackrel{u=t^2}{=} \frac{1}{\sqrt{\pi}} \int_0^{z^2} u^{-\frac{1}{2}} e^{-u} du = \frac{\gamma\left(\frac{1}{2}, z^2\right)}{\sqrt{\pi}}. \quad (\text{S87})$$

Plugging in $z^2 = \frac{r^2}{2\sigma^2}$, we obtain the desired result.

D. Why Gaussian Densities cannot be used in the general case

As was shown in this section, the density contribution functions $g(r)$ have a well-defined limit as $r \rightarrow 0$. Naively, just as for the Coulombic special case, one could hope to achieve this by using the effective potential generated by a Gaussian charge density. This, however, would not work for $p \geq 3$.

The qualitative way of seeing this is to work in spherical coordinates and study the asymptotic scaling of the potential as $r \rightarrow 0$. While the bare $1/r$ potential has a singularity at the origin, the Coulomb potential generated by a Gaussian charge (or any continuous charge density for that matter) is still finite at the origin due to the extra factor of r^2 arising from the Jacobian in spherical coordinates. More generally, $1/r^p \cdot r^2 = r^{2-p}$ can be integrated without leading to singularities as long as $p < 3$. Thus, if we wish to have a set of densities $g_p(r)$ that also varies smoothly with respect to p , it is impossible to use Gaussian densities.

Instead, if we consider the effective $1/r^p$ potential generated by a spherically symmetric density $\rho(\mathbf{r})$, the potential at a point \mathbf{r} is then given by

$$\phi(\mathbf{r}) = \int_{\mathbb{R}^3} \frac{\rho(\mathbf{r}')}{\|\mathbf{r} - \mathbf{r}'\|^p} = \frac{2\pi}{(2-p)r} \int_0^\infty dr' r' \rho(r') [|r - r'|^{-p+2} - (r + r')^{-p+2}] \quad (\text{S88})$$

In our case, $\phi(\mathbf{r})$ would correspond to the density contribution function $g(\mathbf{r})$. Using the specific form in Equation (S76), one can invert the relation and compute what the effective charge density (or smearing) $\rho(r)$ would need to be to get this specific effective density.

S4. HIGHER ORDER DESCRIPTORS AND MANY-BODY EFFECTS

While the main text has mostly focused on LODE and LR interactions as a 2-body interaction, we discuss in this section how the same coefficients can also be combined to produce higher order descriptors containing general n-body information.

A. Review of Invariant Descriptors

We start with a brief review of the analogous results for SR descriptors, and then translate the results to LODE. Since the early successful ML models for the energy of a system,^{3,13} much effort has been dedicated to searching for ways to describe the local environment of an atom in a way that is invariant under translations and rotations. Well-known geometrical descriptors having these properties are the interatomic distances (2-body), angles (3-body) and dihedrals (4-body). Thus, many of the earlier ML models explicitly used these as inputs. In parallel, driven by the popularity of the SOAP descriptor,⁴ a range of descriptors based on the density ρ as introduced in section S2 have been developed and systematically extended. In particular, if we start from the coefficients $\rho_{i,nlm}$ of the density, also written as $\langle nlm | \rho_i \rangle$ in other works and explained in more detail in section S2 (see Eq. (S50)), one can generate a systematic hierarchy of rotationally invariant descriptors by taking polynomial combinations of these coefficients, which is the key idea underlying the implementation of methods like ACE⁶ and NICE.¹⁴ In particular, it was shown that the invariant coefficients linear, quadratic and cubic in ρ contain 2-, 3- and 4-body information, and hence correspond to the distances, angles and dihedrals introduced above. Furthermore, beyond these geometrically interpretable quantities, one can more generally combine ν such coefficients to build a descriptor that contains $\nu + 1$ -body information (the intuition being that the center atom i is given, and each copy of ρ adds one neighbor atom, which is why it is $\nu + 1$ rather than just ν). More explicitly, the invariant descriptors at the linear ($\nu = 1$, 2-body) and quadratic ($\nu = 2$, 3-body) level are given by

$$I[\rho]_n = \rho_{i,n00} \quad (\text{S89})$$

$$I[\rho \otimes \rho]_{nn'l} = \sum_{m=-l}^l \rho_{nlm} \rho_{n'lm} \quad (\text{S90})$$

When used as descriptors in a linear regression model, this family of local coefficients can be used as a basis to expand in a symmetry-adapted way any invariant function of the coordinates of 1, 2, 3, ... neighbors.

Moving to LODE, the coefficients $V_{i,nlm}$ are defined completely analogously to $\rho_{i,nlm}$. In particular, their transformation behavior under rotations of the system is exactly the same, arising from the properties of the spherical

harmonics. In particular,

$$I[V]_n = V_{i,n00} \quad (\text{S91})$$

$$I[V \otimes V]_{nn'l} = \sum_{m=-l}^l V_{nlm} V_{n'lm} \quad (\text{S92})$$

are the simplest invariants one can build corresponding to $\nu = 1, 2$, while expressions for $\nu \geq 3$ also involve Clebsch-Gordan coefficients, corresponding to the expressions for the density bispectrum.¹⁵ Arbitrary-order equivariant descriptors, involving combinations of short and long-range terms, can be obtained with an iterative procedure as discussed in Refs. 16,17 for the case of the short-range atom-centered density correlations.

B. Interpretation of LODE coefficients in Terms of Many-Body Interactions

We will now show how a linear model built on the descriptors $I^{(\nu)}$ can be interpreted as a parametric family of $\nu+1$ -body functions. For simplicity, we will write the results in this section by using the energy E as a target property, but the argument would equally apply to any other target property that is invariant under rotations. We will assume a general interaction exponent p throughout this section. Furthermore, we will assume that only the atoms (density) outside of the cutoff radius generates the potential, since it is the exterior part that we wish to capture with LODE (the interior part can be subtracted using more conventional methods).

We first discuss the two cases $\nu = 1, 2$ separately, and follow with the general calculation. Starting with $\nu = 1$, it was shown in section S1 that the information content in the coefficients $V_{i,nlm}^>$ essentially corresponds to the exterior multipole moment $M_{i,nlm}^>$ defined as

$$M_{i,nlm}^> \propto \int_{r_{\text{cut}}}^{\infty} d^3\mathbf{r}' \frac{\rho(\mathbf{r}')}{r'^{p+l+2n}} \quad (\text{S93})$$

and in particular for $l = m = 0$:

$$M_{i,n00}^> \propto \int_{r_{\text{cut}}}^{\infty} d^3\mathbf{r}' \frac{\rho(\mathbf{r}')}{r'^{p+2n}} \quad (\text{S94})$$

This, however, is just the total $1/r^{p+2n}$ potential generated by the exterior charges. This can be made even more explicit by assuming that the density $\rho = \sum_j q_j \delta(\mathbf{r} - \mathbf{r}_{ij})$ is made up of point particles containing charges q_j , in which case we get

$$M_{i,n00}^> \propto \sum_j \frac{q_j}{r_{ij}^{p+2n}}, \quad (\text{S95})$$

where we have more explicitly written $r_{ij} = |\mathbf{r}_j - \mathbf{r}_i|$ to emphasize that we are working in a coordinate system centered around some atom i . Thus, if we use a linear model built on these features to predict, say, the ‘‘atomic energy’’ ϵ_i of a system, this corresponds to

$$\epsilon_{i,\text{pred}} = \sum_n \tilde{c}_n M_{i,n00}^> = \sum_j q_j \sum_n c_n \frac{1}{r_{ij}^{p+2n}}, \quad (\text{S96})$$

where we have absorbed some proportionality constants into the definition of c_n . The last form makes it particularly clear that we are effectively fitting the total energy using a linear combination of $1/r^p, 1/r^{p+2}, 1/r^{p+4}, \dots$ up to some maximal exponent. We thus obtain a model that predicts energies as a linear combination of 2-body terms.

Moving on to the quadratic case, $\nu = 2$, we consider a linear model built on

$$I[V \otimes V]_{nn'l} = \sum_{m=-l}^l V_{nlm} V_{n'lm}. \quad (\text{S97})$$

Writing only the basis functions that can be combined with the appropriate fitting coefficients, this is equivalent to an expansion in terms of the products of the multipole moments

$$\sum_m M_{i,nlm}^> M_{i,n'lm}^> = \sum_m \int_{r_{\text{cut}}}^{\infty} d^3\mathbf{r}' \int_{r_{\text{cut}}}^{\infty} d^3\mathbf{r}'' \frac{\rho(\mathbf{r}')}{r'^{p+l+2n}} \frac{\rho(\mathbf{r}'')}{r''^{p+l+2n'}} Y_l^m(\mathbf{r}') Y_l^m(\mathbf{r}'') \quad (\text{S98})$$

Using the spherical harmonics addition theorem,

$$\frac{4\pi}{2l+1} \sum_m Y_l^m(\hat{\mathbf{r}}_1) Y_l^m(\hat{\mathbf{r}}_2) = P_l(\hat{\mathbf{r}}_1 \cdot \hat{\mathbf{r}}_2), \quad (\text{S99})$$

we can rewrite the above as

$$\sum_m M_{i,nlm}^> M_{i,n'lm}^> = \int_{r_{\text{cut}}}^{\infty} d^3\mathbf{r}' \int_{r_{\text{cut}}}^{\infty} d^3\mathbf{r}'' \frac{\rho(\mathbf{r}')}{r'^{p+l+2n}} \frac{\rho(\mathbf{r}'')}{r''^{p+l+2n'}} P_l(\hat{\mathbf{r}}_1 \cdot \hat{\mathbf{r}}_2) \quad (\text{S100})$$

Again, taking the limit in which the density $\rho_i = \sum_j q_j \delta(\mathbf{r} - \mathbf{r}_{ij})$ is built as a sum of delta distributions, we obtain

$$\sum_m M_{i,nlm}^> M_{i,n'lm}^> = \sum_{j,k} \frac{q_j q_k}{r_{ij}^{p+l+2n} r_{ik}^{p+l+2n'}} P_l(\hat{\mathbf{r}}_{ij} \cdot \hat{\mathbf{r}}_{ik}). \quad (\text{S101})$$

This form makes clear that the invariant component corresponding to the indices n, n', l corresponds to a 3-body interaction

$$V_{nn'l}^{\text{3-body}}(r_{ij}, r_{ik}, \theta_{jk}) = \frac{1}{r_{ij}^{p+l+2n} r_{ik}^{p+l+2n'}} P_l(\cos \theta_{jk}) \quad (\text{S102})$$

parametrized by the two sidelengths r_{ij} , r_{ik} of the triangle formed by atoms i, j, k , as well as the angle θ_{jk} between these sides formed at the position of atom i . The combinations of multiple coefficients p, l, n provides a family of models that can capture 3-body interactions with arbitrary decay exponents. We will examine the flexibility of the many-body LODE features in the next subsection.

For $\nu = 1, 2$, we have explicitly written out the radial and angular dependencies of the resulting potential. While the angular part becomes more complicated for higher order invariants, the general intuition remains the same. By combining ν multipole moments characterized by (p_1, n_1, l_1) , (p_2, n_2, l_2) , \dots , (p_ν, n_ν, l_ν) , one can build invariant coefficients representing an $\nu + 1$ -body interaction with arbitrary decay exponents with respect to neighbor distances, and complex dependencies on the relative spatial arrangements of far-field atoms.

C. Results on Many-Body Dispersion

1. Fitting DFT Data

We now show how a linear model only built on $\nu = 1$ invariants can not learn the 3-body part of many-body dispersion, while a model also using $\nu = 2$ can. We generated a dataset consisting of 100 Xenon dimers, as well as 100 Xenon trimers in which the three atoms are placed on an equilateral triangle. For both, the distance d between the atoms (the side length of the triangle for the trimers) has been varied between 3.5 and 14 Å. The energies of the molecules were computed using the identical settings as for the molecular dimers discussed in [section S6 A](#).

We then learn these energies using a linear model including two different features: only the invariants linear in the LODE coefficients, $I[V]_n$, which describe pair interactions, as well as the quadratic invariants $I[V \otimes V]_{nn'l}$ that contain 3-body information. The models are trained on a subset of the entire dataset only containing the molecules up to the cutoff separation of 7.5 Å, the results of which are shown in [Figure S6](#). The left column (subfigures a and c) shows the results of the first model only using the two-body descriptors, while the right column (subfigures b and d) uses a model that uses both two- and three-body LODE features.

Superficially, just comparing the panels (a) and (c) showing the total energy of the dimers and trimers, the two models seem to yield similar performance. The difference becomes clear, however, once we compare the accuracy on the three-body part of the energy, shown in panels (b) and (d). We see in (b) that the two-body model cannot learn the three-body part of the energy at all, while in (d), we see that a model which includes three-body LODE features can capture the behavior well. Moreover, looking at the scale of the energy shows that the three-body part of the energy is less than a tenth of the total energy. Thus, the apparent good performance of the two-body-only model seen in panel (a) is simply due to the fact that the dominant two-body component was captured well. Higher accuracies, however, clearly need to capture the three-body part as well, requiring the use of the higher order LR features.

2. Model Details

For the two-body features, we used a potential exponent $p = 6$ to match the leading term of dispersion interaction, with a monomial basis consisting of $n_{\text{max}} = 6$ basis functions and a smearing parameter of $\sigma = 1$ Å. For the three-body

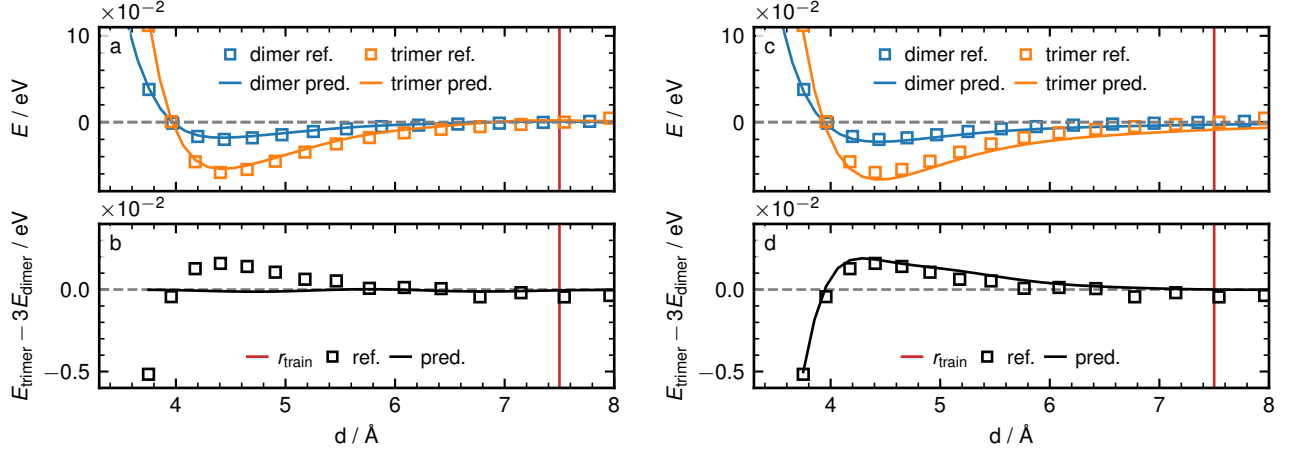


Figure S6. Fitting of three-body dispersion using LODE. The two figures on top (a,c) show the target data and predicted curves for the total energy of both the dimers and trimers as a function of the interatomic distance d . The two figures on the bottom (b,d) show the analogous result for the three-body part of the energy, defined as $E_{3b}(d) = E_{\text{trimer}}(d) - 3E_{\text{dimer}}(d)$. For the left hand column, a linear model only using two-body features is used, which fails to capture the three-body part as shown in panel (b). On the right hand column, a three-body LODE features are used as well, leading to a model that can also capture the three-body part of the energy.

features, we used the same radial basis, $p = 4$ (such that the effective decay potential $2p = 8$ is close enough to the theoretical asymptotic value of 9, which corresponds to the total exponent in the Axilrod-Teller-Muto potential, that is often used to describe 3-body dispersion interactions), $l_{\text{max}} = 4$ and $n_{\text{max}} = 6$. The learning was performed using the ridge regression class of scikit-learn with regularization parameter $\alpha = 10^{-12}$.

Since the two atoms for the dimers and three atoms for the trimers have the exactly same environment (up to rotations), these will have the same rotationally invariant descriptors $I[V]_n$ and $I[V \otimes V]_{nn'l}$ (recall that $I[V \otimes \dots \otimes V]$ with ν factors contains $\nu + 1$ -body information). The model can thus be effectively written as

$$E_{\text{pred}}^{(2b)} = 2 \sum_{n=0}^{n_{\text{max}}-1} w_n^{(2)} I[V]_n \quad (\text{S103})$$

$$E_{\text{pred}}^{(3b)} = 3 \left(\sum_{n=0}^{n_{\text{max}}-1} w_n I[V]_n + \sum_{n,l,l'} w_{n,n',l}^{(3)} I[V \otimes V]_{nn'l} \right) \quad (\text{S104})$$

with model parameters $w_n^{(2)}$ and $w_{n,n',l}^{(3)}$, and the same loss function as in [section S5](#).

3. Fitting the ATM Potential

A commonly used many-body potential, representing the first correction to the two-body description of dispersion, is the Axilrod-Teller-Muto (ATM) potential, which between three particles labelled as i, j, k is explicitly given by

$$V^{\text{ATM}} = \frac{1 + 3 \cos \theta_i \cos \theta_j \cos \theta_k}{(r_{ij} r_{ik} r_{jk})^3}. \quad (\text{S105})$$

We now examine to which extent this ATM potential can be captured exactly for the simple special case in which i, j, k form an isosceles triangle with the common sides meeting at i . In this case, the geometry is specified by two parameters d , the common side length, and $\theta = \theta_i$. The potential can then be written as

$$V^{\text{ATM}}(d, x) = \frac{1}{d^9} \frac{1 + \frac{3}{2}x(1-x)}{(2(1-x))^{3/2}}, \quad (\text{S106})$$

where $x = \cos \theta$. If we wish to fit this using a superposition of the 3-body LODE features as shown in Eq. (S102), we need to only consider terms in which the total decay exponent $p + p' + 2l + 2n + 2n' = 9$, where in general, it is

possible to combine coefficients arising from different values of p, n, n' . Since $p, n \geq 0$ (where n is an integer and p is a real number), this provides us with a restriction of the form $2l \leq 9$ which has the solutions $l = 0, 1, 2, 3, 4$, leading to angular dependencies of the form $P_l(\cos \theta) = P_l(x)$ with $x = \cos \theta$ as before. In other words, a general LODE model with a total asymptotic decay of $1/r^9$ can capture any angular dependence that is a linear combination of the first five Legendre polynomials. For the ATM potential which is the leading three-body term, this means to approximate

$$V^{\text{ATM}}(d, x) = \frac{1}{d^9} \frac{1 + \frac{3}{2}x(1-x)}{(2-2x)^{3/2}} \approx \sum_{l=0}^4 \tilde{w}_l P_l(x) = \sum_{l=0}^4 w_l x^l \quad (\text{S107})$$

for some fitting coefficients \tilde{w}_l (in terms of the Legendre polynomials) or w_l (in terms of the standard monomials).

In [Figure S7](#), we show the results of this fit (where ‘‘best fit’’ is defined in the L_2 -sense) for ranges of the angle θ : $\theta \in [\pi/4, \pi] = [45^\circ, 180^\circ]$ in panel (a) and $\theta \in [\pi/9, \pi] = [20^\circ, 180^\circ]$ in panel (b). The initial cutoff angle of 45° corresponds to the angle formed at the position of a center atom i , if the two neighbors are at a distance of 4 \AA from i and 1.5 \AA from each other, thus corresponding to the three-body contribution by a pair of atoms ‘‘right outside the cutoff’’ radius. We can see that if we restrict the range of the angle as shown in (a), we obtain a good fit of the angular dependence of the ATM potential. On the other hand, if we also include narrower angles as shown in (b), we can see that the potential starts to diverge, and the performance of the fit becomes more restricted.

The difficulty in fitting the divergent part will not be a huge issue in practice due to its origin: it should be noted that this divergence arises from the factor of $1/r_{jk}^3$ as $r_{jk} \rightarrow 0$. In other words, as the two atoms ‘‘around’’ atom i approach each other. If the two atoms in practice are closer than the cutoff radius, the SR part of the model would be strongly affected by it, and adapt its coefficients to learn that part of the interaction (at least to the extent that SR models can do that, since such short-distance divergences are also challenging for conventional ML Models).

To make this more explicit: naively, the angle θ at the position i could be small even if the atoms j, k have a more reasonable distance a , if the distance $d \rightarrow \infty$ goes to infinity. We however know that for an isosceles triangle, $2a = d \sin \theta/2$ and thus as $d \rightarrow \infty$, the angle θ will asymptotically approach $\theta \sim \frac{4a}{d} + O((\frac{a}{d})^3)$. In this limit, we then get the asymptotic result

$$V^{\text{ATM}} \sim \frac{1}{d^9} \frac{1}{(\sin \frac{\theta}{2})^{3/2}} \sim \frac{1}{d^6 a^3}. \quad (\text{S108})$$

which is precisely the distance dependence of the ATM potential for three particles forming a triangle with side lengths d, d, a , showing also directly using the angle dependence that there is no true singularity. Furthermore, for $d \rightarrow \infty$, the far-field contributions of the comparably quickly decaying $1/r^9$ potential will only constitute a tiny fraction of the total energy. The most dominant part of such a three-body correction would arise from atoms that are right outside of the cutoff radius, and for those, the angle θ will be limited by the small value of d (for instance, two neighbors are at a distance of 4 \AA from the center and 1.5 \AA from each other would form an angle of 45° , which was the value chosen for [Figure S7](#)). This simple toy example shows that the three-body extension of LODE is capable of capturing this interaction decently well.

S5. MODEL DETAILS FOR THE POINT-CHARGE TOY PROBLEM

The toy dataset comprised of a gas of point particles interacting through pure electrostatic or dispersion interactions is built following the procedure discussed in the main text and in [Ref. 11](#). For each structure we compute the atom centered spherical expansion where we use a single angular channel ($l = 0$ and hence automatically $m = 0$), one radial channel for the optimized (monomial) basis, and eight radial channels for the GTO basis. For the short range (SR) model we use a rather large cutoff of 9 \AA and set the width of the Gaussian densities to $\sigma = 1 \text{ \AA}$. For the long-range (LR) LODE model we use an environment cut-off 0.1 \AA and a Gaussian width of 0.6 \AA . In all cases, we predict the total energy of a structure using a decomposition

$$E_{\text{pred}} = \sum_{i=1}^N \epsilon_i, \quad (\text{S109})$$

where ϵ_i is the predicted atomic energy for atom i , which is in turn expressed as

$$\epsilon_i = \begin{cases} \sum_{n=0}^{n_{\text{max}}-1} \sum_a w_{na} V_{i,an00} & \text{LODE} \\ \sum_{n=0}^{n_{\text{max}}-1} \sum_a w_{na} \rho_{i,an00} & \text{SR} \end{cases}, \quad (\text{S110})$$

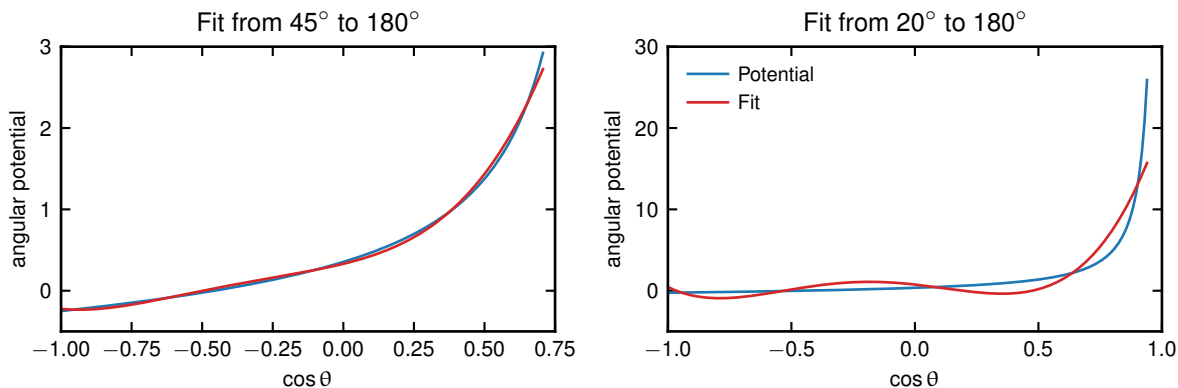


Figure S7. Fitting of angular part of the ATM potential, the equation of which is provided in the text. The fit is performed on two interval ranges for the angle θ : $\theta \in [\pi/4, \pi] = [45^\circ, 180^\circ]$ in panel (a) and $\theta \in [\pi/9, \pi] = [20^\circ, 180^\circ]$ in panel (b). The initial angle of 45° corresponds to the angle formed at the position of a center atom i , if the two neighbors are at a distance of 4 \AA from i and 1.5 \AA from each other, thus corresponding to the three-body contribution by a pair of atoms “right outside the cutoff” radius.

where a runs over all species present in the system, and w_{an} are model weights. We use $n_{\max} = 8$ for the GTO radial basis (used for both SR and LODE features) while $n_{\max} = 1$ for the optimized (monomial) radial basis of LODE.

The weights are optimized by performing a simple ridge regression against the energy, i.e. by minimizing the loss function

$$\mathcal{L}(\mathbf{w}) = \sum_A (E(A) - E_{\text{pred}}(A))^2 + \lambda \sum_n w_n^2, \quad (\text{S111})$$

where $E(A)$ is the energy of structure A , $\mathbf{w} = (w_0, w_1, \dots)$ is the vector of weights and λ is a regularization parameter. The actual optimization is performed using the implementation in Scikit-learn,¹⁸ with a regularizer of $\lambda = 1 \cdot 10^{-5}$. Given the linear nature of the model, we compute global descriptors of the structure by summing over all atom-centered descriptors within each structure, and apply the regression algorithm at the structure level.

S6. COMPUTATIONAL DETAILS FOR THE DIMER DATASET

As discussed in the main text, we use a dataset based on the BioFragment Database (BFDb),^{11,19} that contains rigid-molecule binding curves for pairs of molecular fragments that are charged (C), polar (P) or apolar (A), which gives rise to six classes of dimer interactions. In Table S1 we show some general properties of the dataset while in Table S2 we show molecular formula and additional information about the monomers appearing in the dataset.

Table S1. The six classes of dimer interactions, their number of sample in the dataset as well as the standard deviation of the energies and forces of the the training set at a training cutoff of $r_{\text{cut}} = 4 \text{ \AA}$.

Classes	# samples	σ_{energy} meV	σ_{force} meV/Å
CC	2,392	983.72	246.59
CP	3,471	243.00	131.31
PP	2,093	65.70	39.69
CA	2,730	46.43	25.28
PA	5,434	22.10	7.75
AA	13,663	15.10	3.44
Total	29,783		
Total	29,783		

Table S2. Molecular information about monomers together with how many dimers they appear in the total dataset with which another monomer class.

Molecular formula	Label	-C	-P	-A
$C_3N_3H_{10}^+$	C	208	26	65
$C_2O_2H_3^-$	C	4,134	1,053	442
$C_2N_3H_8^+$	C	1,729	234	286
C_2H_6	A	780	1,716	22,490
C_2ONH_5	P	416	2,639	455
$C_4N_2H_6$	P	208	1,261	377
C_3ONH_7	P	78	455	195
C_3H_8	A	312	572	4,836
CNH_6^+	C	624	117	0
$C_2OH_6^-$	C	130	949	416
$C_3O_2H_5$	P	806	169	429
$C_5N_2H_8$	P	39	117	39
C_9NH_9	P	0	78	0
COH_4	P	442	1,456	117
C_7H_8	A	182	195	3,770
C_3OH_8	A	78	182	117
C_7OH_8	A	234	1,742	819
C_2NH_8	A	507	39	117
C_4H_{10}	P	52	52	507
$C_5ONH_{11}^-$	C	13	26	0
C_8H_{10}	P	13	0	13
C_8OH_{10}	P	0	13	0

A. Reference energy calculations

We orient the dimers in a periodic cell with a length of 30 Å so that the connecting vector between the COMs of the two fragments points in the (1, 1, 1) direction of the cell. Binding energies and forces are calculated using the Heyd, Scuseria, and Ernzerhof (HSE06)²⁰ hybrid functional together with a non-local many-body dispersion correction to handle the LR van der Waals (vdW) energy as implemented in the FHI-Aims package.²¹ For the HSE06 functional, we split the exchange energy into 75 % Hartree-Fock and treat the remaining 25 % at the PBE level.

B. Empirical interaction exponents

To extract the empirical decay exponents p_{phys} for the interaction energy from the data set we fit each binding curve individually to a linear function on a double logarithmic scale. The linear fit function has the form $f(r) = p_{\text{phys}} \cdot r + b$, where f can either be the energy E or the magnitude of the molecular force $|F_{\text{mol}}|$. The molecular force is defined as the sum of all forces acting on the atoms of each molecule (for a given dimer, the total forces on the two molecules are equal in magnitude and opposite in sign). Figure S8 shows all binding curves of a subset, i.e. CC for charge-charge, as gray solid lines and one representative fit as a solid black line. The mean and standard error of each p_{phys} is given in the legend of each sub-panel. We find that, for every type of interaction, the physical exponent is systematically higher compared to the ideal exponent p_{ideal} . This is an indication of the fact that molecules in the DFT simulation are not ideal point particles as assumed in the derivation of the ideal exponents. Spurious interactions between periodic replicas (especially for charged fragments), as well as noise in the binding energy at large distance (especially for weak interactions) contribute to this discrepancy.

C. SOAP and LODE Hyperparameters

For the SR and the LR spherical expansions we use a cutoff/environment-cutoff of 3.0 Å. For the SR model we use a density Gaussian width of 0.3 Å, and expand the density on a basis including four angular channels, and six GTO-type radial basis channels. The density at the cutoff is smoothed using a shifted cosine switching function with a width of 0.5 Å. For the LR model we either use an optimal monomial basis containing one radial channel and one angular channel, or an extended monomial basis containing six radial and four angular channels, with the

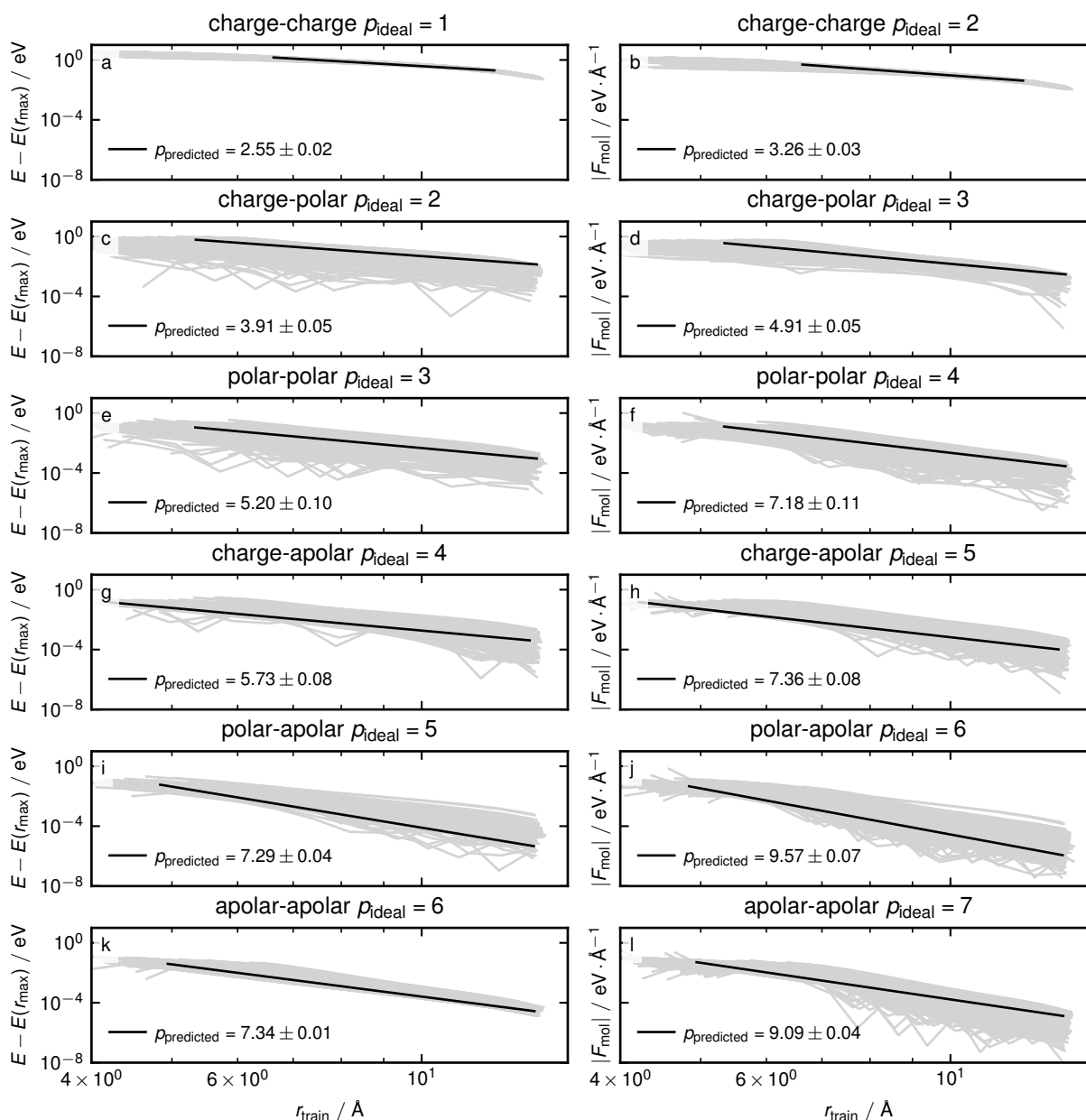


Figure S8. Dimer binding curves on a double logarithmic scale. Gray lines show the binding curves from the DFT simulation and solid black lines shows an example linear fit to a representative binding curve. Values in each figure legend indicate the mean and standard error for each ρ_{phys} . Each row of sub-panels shows binding curves for different subset of the dimers. Left columns: Binding energies $E - E(r_{\text{max}})$. For a better visualization all curves are shifted by the energy at the maximum separation $E(r_{\text{max}})$. Right columns: Absolute molecular force $|F_{\text{mol}}|$.

exponents determined according to the theoretical analysis in [section S2F](#). For the LR descriptors we set the width of the Gaussian basis functions to 1 Å and we use no cosine switching function at the cutoff distance. From the atom centered spherical expansion coefficients of the density and the associated potential we construct the $\rho \otimes \rho \oplus \rho \otimes V_p$ multiscale power spectra according to.¹¹

D. Linear Models: Separate Dimer Classes

We construct linear-regression models for each type of dimers, using global features obtained by summing over all atom-centered descriptors within each structure, supplemented by composition features that representing the chemical stoichiometry of each structure. Explicitly written out, we predict the atomic energy of atom i by

$$\epsilon_i = \begin{cases} \sum_{aa'nn'l} w_{aa'nn'l} I[\rho_i \otimes V_i]_{aa'nn'l} & \text{LODE} \\ \sum_{aa'nn'l} w_{aa'nn'l} I[\rho_i \otimes \rho_i]_{aa'nn'l} & \text{SR,} \end{cases} \quad (\text{S112})$$

where $I[\rho_i \otimes V_i]_{aa'nn'l}$ are the previously mentioned invariants $\sum_m \rho_{i,anlm} \rho_{i,a'n'lm}$ and similarly for $\rho \otimes \rho$ and the total energy is then predicted as the sum of atomic contributions plus an additional species-wise baselining:

$$E_{\text{pred}} = \sum_i \epsilon_i + \sum_a \tilde{\epsilon}_a N_a, \quad (\text{S113})$$

where N_a is the number of atoms of species a , and $\tilde{\epsilon}_a$ is a constant offset in the energy of each such atom. During the linear regression we use a very small regularizer of $2.2 \cdot 10^{-16}$ for the composition features and optimize the regularizer for the SR and LR features using a grid search. The grid is ranges from 10^{-12} to 10^3 and contains 20 equally spaced points. We find the optimal regularizer by minimizing the total RMSE of the energies and forces according to $\text{RMSE} = (\text{RMSE}_{\text{energy}} + \text{RMSE}_{\text{force}})/2$. The linear regression is performed with the `equisolve` packages maintained at <https://github.com/lab-cosmo/equisolve>. Percentage RMSE are computed by normalizing the absolute RMSE values by the standard deviation of the binding energy of the training structures, computed separately for each dimer subset.

E. Atomic Force Errors

In Figure S9 we compare the accuracy of the atomic force on the test set predicted by linear models using multiple monomials for the radial expansion. Similar to what shown in Figure 3b in the main text we compare different potential exponents $p = 1, 2, \dots, 9$ and fit separately on each dimer fragment classes. As for the energy we find that all short-range models suffer from poor performance, and the inclusion of any LODE term leads to dramatic improvement in the test accuracy. However, the improvement is less pronounced than for the energies, and there is less-pronounced variation of the accuracy depending on the generalized LODE exponent, even though we find that the best potential exponent roughly corresponds to the ideal exponents for each dimer class.

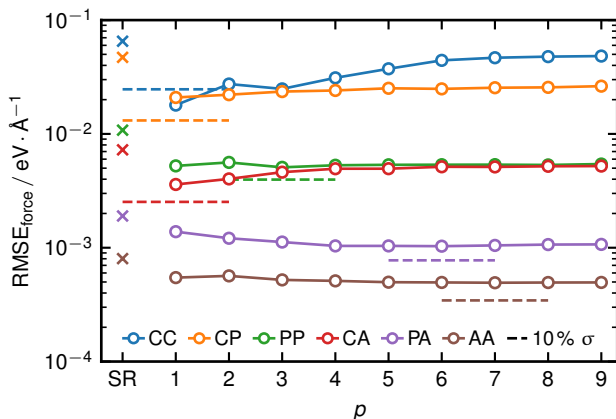


Figure S9. The figure shows the atomic force RMSE as a function of the potential exponent p , similar to Figure 3 in the main text. Dashed horizontal lines depict the RMSE corresponding to 10% σ .

F. Test Errors for Different Training Cutoffs

We recall that the extrapolative learning exercise we perform involves predicting the long-range part of the binding curve, for $r > r_{\text{train}}$, based on training on the part of the data set with $r \leq r_{\text{train}}$ (where distances are defined relative to the minimal separation in the dataset for each dimer configuration). In Figure S10 we show the % RMSE for the

energies and forces for different subsets of the dataset as a function of the training cutoff r_{train} and the potential exponent p . We find that an increased training cutoff increases the accuracy on the test set. We note that due to the construction of our train/test split these curves are not usual learning curves. Contrary to the typical training exercises in which the number of test points remains constant, when the training cutoff is increased the number of training points increases while the number of test points decreases. This leads to a flattening of the RMSE curves as a function of the r_{train} for the shorter range interaction types like polar-polar, charge-apolar, polar-apolar and apolar-apolar. For these subsets their binding energy and force is almost zero if the two molecules are further apart than a few Å. Therefore, the learning accuracy will not increase for even larger r_{train} since the whole energy and force can be fully described by the contributions of the isolated individual molecules. We also note that for the force RMSE we find only very little difference between the long and the short range models. This is due to the fact that the force on individual atoms is dominated by the force exerted by nearby atoms, which is usually not zero because of the fact that the binding curves are computed without relaxing the atoms at each interatomic separation.

From this discussion we conclude that the chosen train-test split of 4 Å, which we use in the rest of this work, is

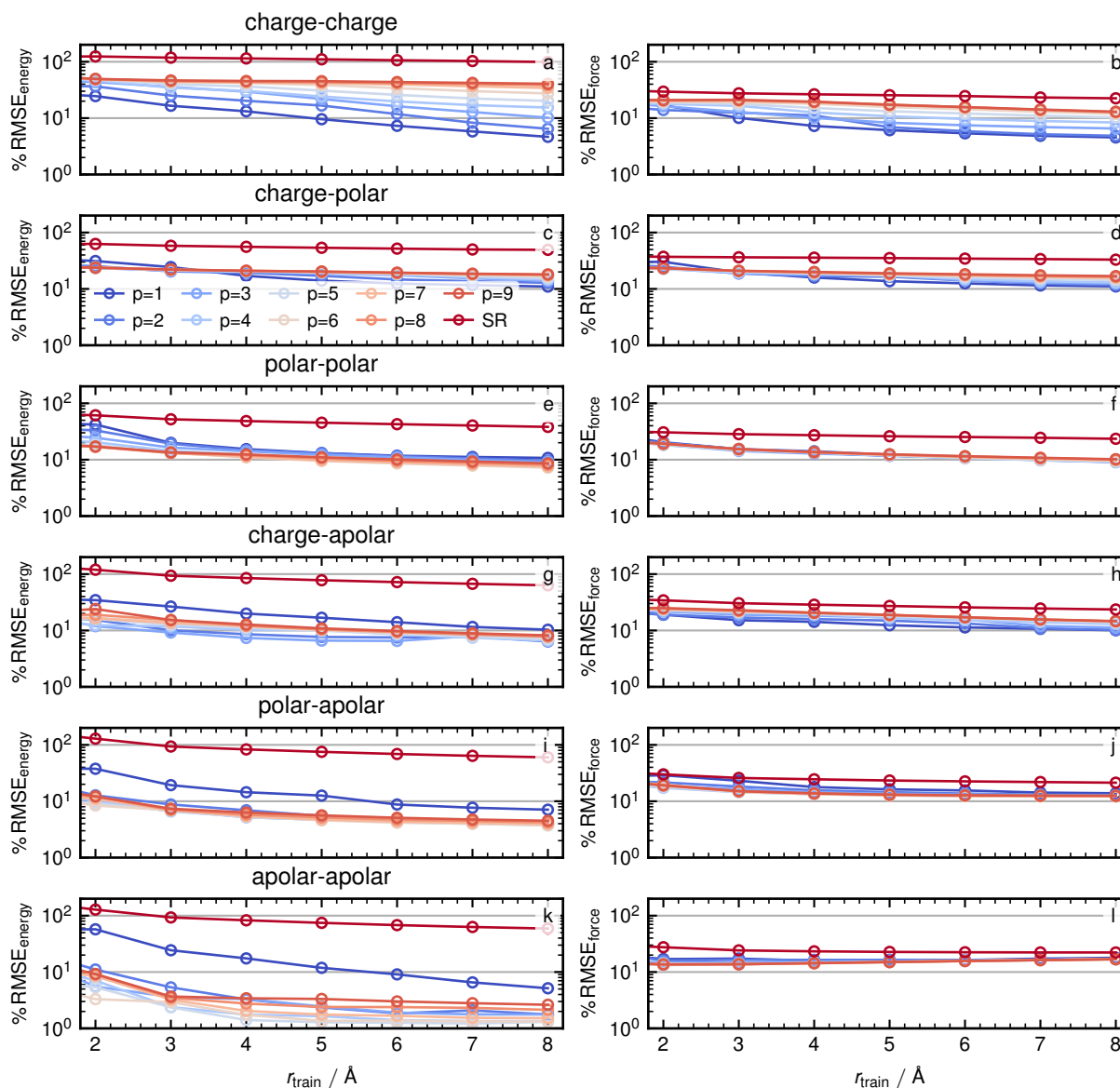


Figure S10. % RMSE for energies and forces for different dimer classes as a function of the training cutoff r_{train} and the potential exponent p . Subpanel titles indicate the corresponding dimer class. Left columns show % RMSE_{energy} while right columns show % RMSE_{force}. Different colors indicate different potential exponents p used in the generalized LODE descriptors.

a reasonable choice since force curves have not already fully flattened out and the train set is sufficiently large for a physically-inspired model to be able to infer the asymptotic behavior of the interactions, and perform reasonable extrapolative predictions on the test set.

G. Energy Errors for Combined Linear Models Using Non-Charged Fragments

In Figure S11 we show the %RMSE of the energy for models trained on several dimer classes simultaneously. However, instead of training on the whole data set, we chose a subset excluding the charge-charge interactions (!CC, black open circles) or all dimer classes that contain some charged fragment (!C, gray open circles). The SR models show a very poor performance even though the slowest decaying $1/r$ interactions are left out. Comparing the black and the gray open circles we find that the model accuracy increases by a factor of two if all charged molecules are excluded from the model. This originates that for the remaining PP, PA and AP classes the standard deviation of the energies are very similar as we show in the legend of Figure 3b in the main text.

Comparing the potential exponent dependence for the training without the charge-charge fragments we find the best model for potential exponent is $p = 2$. This corresponds to the next slowest decaying interaction after CC, and therefore the largest contribution to the energy, that stems from the charge-polar fragments. For the training on the subset without any charged fragments we find a minimum around $p = 4$ which roughly corresponds to the ideal potential exponent of polar-polar interaction, which is 3. In addition, we find that the model accuracy is nearly independent in the range from $p = 2$ to $p = 6$, which is the range of the potential exponents for the PP, PA, and AA pairs. The weak dependence of the accuracy on the exponent for this subset is consistent with the similar weak dependence seen for the separate training exercises, and reflects the fact that (1) these weak interactions have a similar range of variability, so there is little gain in using an exponent optimized for one of the classes, and (2) the weaker interaction often show pronounced deviations from the ideal behavior (Figure S8).

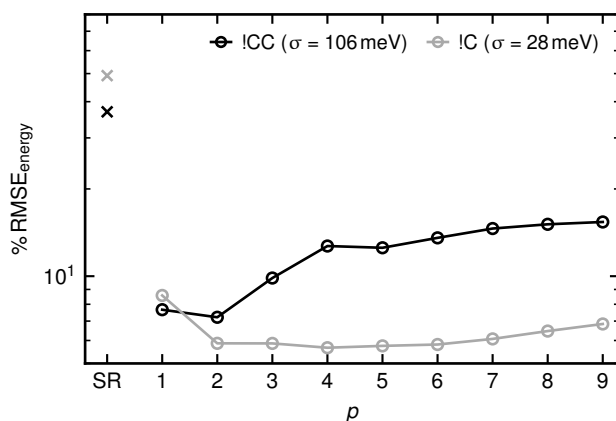


Figure S11. The figure shows the energy %RMSE for models trained on the energies of all dimer structures, up to a cutoff $r_{\text{train}} = 4$ Å, leaving out the CC fragments (!CC, in black) or all the dimers containing a charged residue (!C, in gray, including only PP, PA, AA dimers). The model details and training protocol are analogous to those used for Figure 3 in the main text.

H. Details of the Neural Network Models

We apply a multilayer perceptron neural network (NN) model to the concatenation of SR and LR descriptors at the level of individual environments, summing over the environments to determine the total energy of each structure, that is used as the target property. The NN uses three hidden layers each with 16 neurons. We use a sigmoid linear unit (SiLU) as activation function and perform a layer normalization for each layer. All models were trained using the Adam optimizer²² as implemented in pytorch.²³ The learning rate is reduced by a factor of 0.8 every 1000 epochs if the validation loss reaches a plateau. Means and errors of the RMSE's are obtained from five independent training runs. In Figure S12 we show a bar plot analogous to Figure 4 in the main text, displaying the energy RMSE on the train set for energies and forces for the neural network (NN) models. The figure shows that the additional flexibility afforded by a NN architecture allows to improve the accuracy in the interpolative regime, but is not able to improve the extrapolative performance, that requires a physical prior.

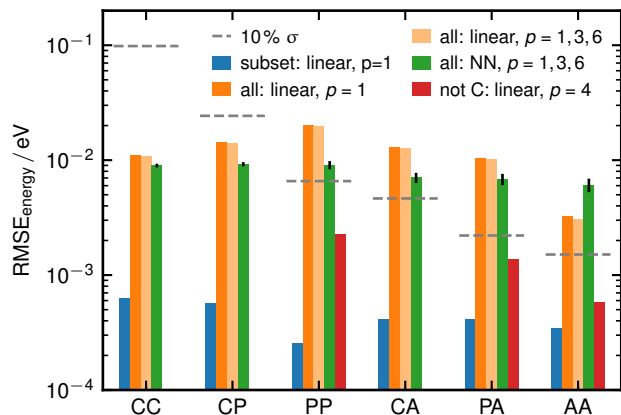


Figure S12. Energy RMSE on the train set for the energies for the different subsets of the dimers. The vertical scale and color coding match those used in Figure 4 in the main text. Blue bars show the RMSE of models using a single $p = 1$ LODE exponent. Orange and light orange bars show linear models fit to the whole data set. Green bars show a fit to the whole data set with a non-linear neural network model. Red bars correspond to a linear model restricted to non-charged fragments. Horizontal gray lines depict an relative error of $10\% \sigma$ for each subset.

I. Relative Energy Errors for Different Subsets

In Figure S13a we plot the relative RMSE in % with respect to the standard deviation in the energies of the training data based on the data of Figure 4 in the main text which shows the error on the test set. Figure S13b shows the relative error on the training set based on the results shown in Figure S12. The figure shows that for a training on the whole dataset the absolute errors on all subsets are comparable, and the main challenge in improving the relative accuracy for the weaker interactions is due the the discrepancy between the energy scale of different long-range effects.

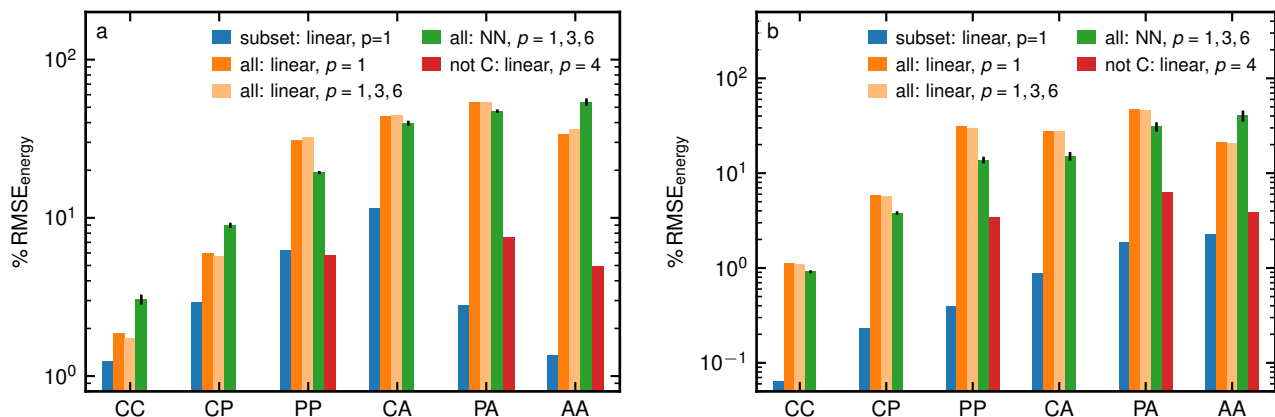


Figure S13. The subsets relative RMSE on the test (a) and the train (b) set for the energies. Blue bars show the RMSE of models using a single $p = 1$ LODE exponent Orange and light orange bars show linear models fit to the whole data set. Green bars show a fit to the whole data set with a non-linear neural network model. Red bars correspond to a linear model restricted to non-charged fragments.

S7. FLEXIBILITY OF POWER-LAW FITS

In this section we show a simple example to illustrate how, given a sufficiently flexible functional form, different types of asymptotic behavior can be achieved using a single potential exponent for the LR features. We consider the following toy model in one dimension: We aim to fit a target function $f(x) = 1/|x|^p$ for fixed p . To do so, we use 6 “atoms” with x coordinates $x \in (-2.5, -1.3, -0.4, 0.5, 1.4, 2.2)$, i.e. atoms around the origin with average distance on the order of 1 roughly corresponding to interatomic distances in Å. We then assume that each of the $i = 1, \dots, 6$ points generates a $1/|x|^{p'}$ potential, where $p' \neq p$ is different from the true exponent, and with “charges” q_i that can be fitted to the data. Thus, we obtain the fitting function

$$\tilde{f}(x) = \sum_{i=1}^6 \frac{q_i}{|x - x_i|^{p'}}. \quad (\text{S114})$$

In Figure S14 a and b, we try to fit a true underlying function $f(x) = 1/|x|$ (i.e. $p = 1$) using a superposition of six $1/|x|^3$ functions (i.e. $p' = 3$). We compare the true function (black solid line) against the obtained least squares fit (red dashed line), where the fit was performed such as to minimize the squared error

$$\text{Loss} = \int_{x_{\min}}^{x_{\max}} |f(x) - \tilde{f}(x)|^2 dx, \quad (\text{S115})$$

where the fitting interval was chosen to be $[x_{\min}, x_{\max}] = [5, 10]$.

In Figure S14a, we can see that in this fitting interval, the six $1/|x|^3$ functions lead to an essentially perfect fit of the true underlying $1/|x|$ potential. However, as we move to figure b, and observe how the fit performs against the true behavior for distances beyond the fitting interval, we can see that fit is not truly capturing the LR $1/|x|$ behavior. In fact, as is expected, the asymptotic behavior of \tilde{f} as $x \rightarrow \infty$ does indeed approach a $1/|x|^3$ form matching the terms in the fitting function.

In Figure S14c and d, we repeat the same exercise but with exponents flipped: the true underlying function (black solid line) is given by $f(x) = 1/|x|^3$, which is fitted by the superposition of six functions decaying as $1/|x|$ (red dashed line). We can again see that the fit is excellent in the fitting interval $x = [5, 10]$ (Figure S14c). A key difference to the previous case, however, is that also in the extrapolative regime d, the fit still remains accurate up to significantly larger distances. In fact, as was shown in much more generality in section S1, it is possible for a superposition of $1/|x|$ potentials to generate a function with an asymptotic behavior of $1/|x|^3$. To provide a simpler example that only requires knowledge about the geometric series, we can use that for $x \rightarrow +\infty$

$$\frac{1}{|x \pm a|} = \frac{1}{x \pm a} = \frac{1}{x} \frac{1}{1 \pm \frac{a}{x}} = \frac{1}{x} \left(1 \mp \frac{a}{x} + \frac{a^2}{x^2} \mp \frac{a^3}{x^3} + \dots \right) = \frac{1}{x} \mp \frac{a}{x^2} + \frac{a^2}{x^3} \mp \frac{a^3}{x^4} + \dots \quad (\text{S116})$$

and thus

$$\frac{1}{|x+a|} + \frac{1}{|x-a|} = 2\frac{a}{x^2} + 2\frac{a^3}{x^4} + \dots \quad (\text{S117})$$

showing that a superposition of two functions decaying as $1/|x|$ can indeed generate a function decaying as $1/|x|^2$, if the relative weights (here, we assumed that the two potentials have the same “charge” / prefactor) and offsets (here: $+a$ and $-a$) lead to a perfect cancellation of the leading $1/|x|$ term. Superpositions of three such functions can then in principle lead to asymptotic $1/|x|^3$ behavior, etc. While possible in principle, this requires a perfect cancellation of terms, which is why the fit in Figure S14(d) does deviate from the perfect $1/|x|^3$ behavior at very large distances.

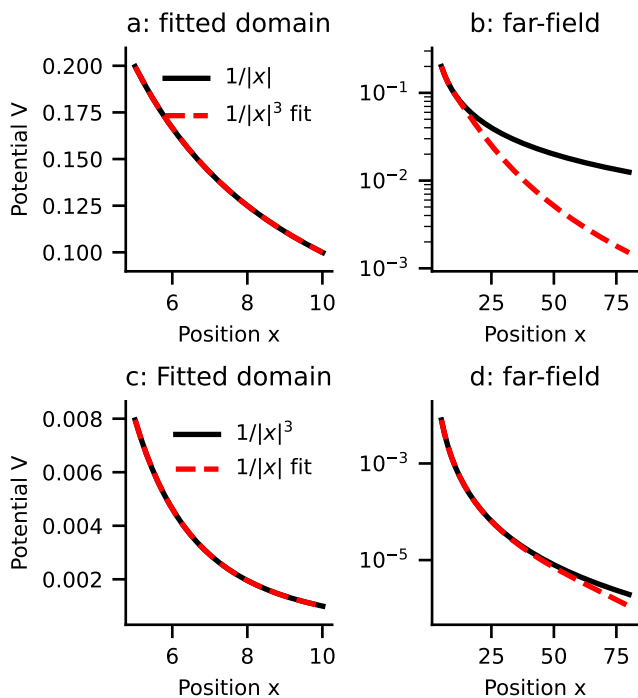


Figure S14. Fitting power law decaying potential with different exponents. Black line shows the to be fitted power law $1/r$ and red dashed line show a fit with a $1/r^3$ power law.

In summary, we can see that restricted to intermediate distances, one can in principle fit any exponent p from any other reasonably close exponent p' , which does not mean that the true far-field behavior is captured. This lack of extrapolation capability for large distances can either be due to fundamental limitations, namely if $p < p'$, or due to the high numerical accuracy that is required to obtain a perfect cancellation of leading order terms for $p > p'$.

We can also flip the story around: if we are only given a superposition of $1/|x|^{p'}$ potentials, e.g. the red dashed lines in the figures S14a and c, and want to find the best $q/|x|^p$ fit for suitable parameters q and p , the exponent we obtain from the fit will typically not be the correct exponent p' unless we can work in the true $x \rightarrow \infty$ limit and no cancellations as discussed above happen (which, in the absence of special symmetries, should only occur with a probability of zero). This shows how the very concept of an “exponent” characterizing a potential can be quite subtle when working with dense systems and a limited dataset.

abbrvnat

-
- (1) Jackson, J. D. *Classical Electrodynamics Third Edition*, 3rd ed.; Wiley: New York, 1998.
 - (2) Musil, F.; Grisafi, A.; Bartók, A. P.; Ortner, C.; Csányi, G.; Ceriotti, M. Physics-Inspired Structural Representations for Molecules and Materials. *Chem. Rev.* **2021**, *121*, 9759–9815.
 - (3) Bartók, A. P.; Payne, M. C.; Kondor, R.; Csányi, G. Gaussian Approximation Potentials: The Accuracy of Quantum Mechanics, without the Electrons. *Phys. Rev. Lett.* **2010**, *104*, 136403.
 - (4) Bartók, A. P.; Kondor, R.; Csányi, G. On Representing Chemical Environments. *Phys. Rev. B* **2013**, *87*, 184115.
 - (5) Behler, J.; Parrinello, M. Generalized Neural-Network Representation of High-Dimensional Potential-Energy Surfaces. *Phys. Rev. Lett.* **2007**, *98*, 146401.
 - (6) Drautz, R. Atomic Cluster Expansion for Accurate and Transferable Interatomic Potentials. *Phys. Rev. B* **2019**, *99*, 014104.
 - (7) Grisafi, A.; Ceriotti, M. Incorporating Long-Range Physics in Atomic-Scale Machine Learning. *J. Chem. Phys.* **2019**, *151*, 204105.
 - (8) Nijboer, B. R. A.; De Wette, F. W. On the Calculation of Lattice Sums. *Physica* **1957**, *23*, 309–321.
 - (9) Williams, D. E. Accelerated Convergence of Crystal-Lattice Potential Sums. *Acta Crystallographica Section A: Crystal Physics, Diffraction, Theoretical and General Crystallography* **1971**, *27*, 452–455.
 - (10) Williams, D. E. Accelerated Convergence Treatment of R-n Lattice Sums. *Crystallography Reviews* **1989**, *2*, 3–23.
 - (11) Grisafi, A.; Nigam, J.; Ceriotti, M. Multi-Scale Approach for the Prediction of Atomic Scale Properties. *Chem. Sci.* **2021**, *12*, 2078–2090.
 - (12) Grisafi, A.; Wilkins, D. M.; Csányi, G.; Ceriotti, M. Symmetry-Adapted Machine Learning for Tensorial Properties of Atomistic Systems. *Phys. Rev. Lett.* **2018**, *120*, 036002.
 - (13) Behler, J.; Parrinello, M. Generalized Neural-Network Representation of High-Dimensional Potential-Energy Surfaces. *Phys. Rev. Lett.* **2007**, *98*, 146401.
 - (14) Nigam, J.; Willatt, M. J.; Ceriotti, M. Equivariant Representations for Molecular Hamiltonians and N-center Atomic-Scale Properties. *J. Chem. Phys.* **2022**, *156*, 014115.
 - (15) Thompson, A.; Swiler, L.; Trott, C.; Foiles, S.; Tucker, G. Spectral Neighbor Analysis Method for Automated Generation of Quantum-Accurate Interatomic Potentials. *Journal of Computational Physics* **2015**, *285*, 316–330.
 - (16) Willatt, M. J.; Musil, F.; Ceriotti, M. Atom-Density Representations for Machine Learning. *J. Chem. Phys.* **2019**, *150*, 154110.
 - (17) Nigam, J.; Pozdnyakov, S.; Ceriotti, M. Recursive Evaluation and Iterative Contraction of N -Body Equivariant Features. *J. Chem. Phys.* **2020**, *153*, 121101.
 - (18) Pedregosa, F. et al. Scikit-Learn: Machine Learning in Python. *Journal of Machine Learning Research* **2011**, *12*, 2825–2830.
 - (19) Burns, L. A.; Faver, J. C.; Zheng, Z.; Marshall, M. S.; Smith, D. G. A.; Vanommeslaeghe, K.; MacKerell, A. D.; Merz, K. M.; Sherrill, C. D. The BioFragment Database (BFDb): An Open-Data Platform for Computational Chemistry Analysis of Noncovalent Interactions. *J. Chem. Phys.* **2017**, *147*, 161727.
 - (20) Heyd, J.; Scuseria, G. E.; Ernzerhof, M. Hybrid Functionals Based on a Screened Coulomb Potential. *J. Chem. Phys.* **2003**, *118*, 8207–8215.
 - (21) Blum, V.; Gehrke, R.; Hanke, F.; Havu, P.; Havu, V.; Ren, X.; Reuter, K.; Scheffler, M. Ab Initio Molecular Simulations with Numeric Atom-Centered Orbitals. *Computer Physics Communications* **2009**, *180*, 2175–2196.
 - (22) Kingma, D. P.; Ba, J. Adam: A Method for Stochastic Optimization. 2017.
 - (23) Paszke, A. et al. PyTorch: An Imperative Style, High-Performance Deep Learning Library. 2019.